LBL-7192

EMISSION OF HEAVY CHARGED PARTICLES IN RELATIVISTIC NUCLEUS-NUCLEUS COLLISIONS

John David Stevenson
(Ph. D. thesis)

December 1977

Prepared for the U. S. Department of Energy
under Contract W-7405-ENG-48

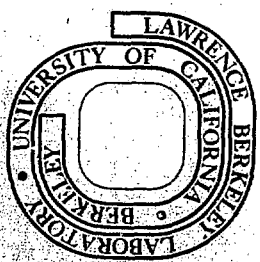

LBL-7192

[illegible]

by John David Stevenson

Abstract

The energy and angular distributions of nuclei produced in interactions of 500 MeV/nucl ^{40}Ar projectiles with an Au target have been investigated. Nuclei with charge $3 \leq Z \leq 11$ were observed. Single particle inclusive spectra have been obtained at angles between 7° and 85°, in the energy range 20 to 60 MeV/nucl.

The spectra decrease monotonically with the increasing energy, angle, and charge. The distributions are consistent with an isotropically emitting source recoiling with an average velocity of ~0.08 c in the beam direction. Thermal model fits to the data yield temperatures τ of about $\tau \sim 60$ MeV. The low recoil velocity and high temperature are shown to be in conflict with energy and momentum conservation. Two non-thermal models of emission involving expansion or rotation are explored. Although neither of these models gives good quantitative fits to the data, they do much better than the thermal model if it is constrained to be energy and momentum conserving.

The data for all energies, angles and species may be simply parameterized. When transformed into a recoiling source frame with

$\beta_o \simeq 0.08$, all data points lie near ($\pm 4x$) a common curve, for which the invariant cross section, $f \equiv \frac{1}{p} \frac{d^2\sigma}{d\Omega dE}$, falls exponentially with increasing momentum, $f \propto e^{-p/p_c}$, with a characteristic momentum $p_c \simeq 340$ MeV/c.

Acknowledgments

I would particularly like to thank Professor P. Buford Price for helpful advice and encouragement. His willingness to patiently read and reread my thesis was an immeasurable aid to me. I would also like to thank other members of the Price group, Ken Frankel, Ed Shirk, and Greg Tarlé, for cheerfully providing technical aid and advice.

Fred Lothrup and the staff of the Lawrence Berkeley Laboratory Bevalac deserve special thanks for providing our group with the world's first high intensity, relativistic ^{40}Ar beam.

I am also grateful to Judy Blair for her skillful typing of my thesis.

Finally I would like to thank the U.S. Energy Research and Development Administration for providing financial support of the work described in this thesis.

$\pi(t,\ell)$, is given by

$$\pi(t,\ell) = \frac{1}{N(\ell)} \exp\left[-(t-\tau(\ell))/\sigma^2(\ell)\right] \tag{11}$$

where $N(\ell)$ is a normalization constant and $\tau(\ell)$ and $\sigma(\ell)$ are the average lifetime and variance of the lifetime distribution for angular momentum ℓ, and

$$\tau(\ell) = \tau(0)(1-\ell/\ell_{max}) \quad , \tag{12}$$

$$\sigma^2(\ell) = \sigma^2(0)(1-\ell/\ell_{max}) \quad , \tag{13}$$

where $\tau(0)$ and $\sigma(0)$ are the values for $\ell = 0$. The quantities $\tau(0)$ and $\sigma(0)$ are taken as adjustable parameters.

Since other processes are observed in heavy ion collisions limits must be placed on the range of ℓ-values contributing to deep-inelastic collisions. Figure 36 is a schematic view of the fractionation of the ℓ-distribution with respect to the various processes. At low ℓ-values the nuclei may fuse into a compound nucleus which can decay either by the emission of light particles (i.e. n,p,α, etc.) or by fission. For very heavy systems like $^{197}Au + ^{86}Kr$ no evaporation residues have been observed (which would border on the realm of superheavy nuclei). For lighter systems (e.g. Ag + Kr) evaporation residues have been observed, but the cross section is small (< 100 mb).[105] Fission following fusion is a rather improbable process for Au + Kr, as evidenced by the Z-distributions which tend to peak near Z = 36, but may occur for Ag + Kr for the low ℓ-waves as previously discussed. In the calculations no lower ℓ-cutoff is assumed for compound nucleus production; however, the

Introduction

High energy collisions between nuclei typically produce a bewildering variety and number of particles, pions, nucleons, and light nuclei. If a heavy target nucleus is used, charged particle multiplicities frequently exceed 50,[1,2] with perhaps a similar number of unseen neutrons and gammas.

One idea that has proven very useful in the analysis of relativistic nucleus-nucleus collisions is that they proceed by formation of a small number of discrete objects which subsequently decay into the large number of fragments seen in the lab.

A common type of collision, which is thought to be peripheral or grazing in nature, is one in which all fragments appear to have been emitted from either the target or the projectile. Target fragments are isotropically emitted in the lab with a relatively small amount of energy, and projectile fragments are emitted in a narrow cone at 0° with velocities very near the beam velocity.[3,4,5] However, frequently collisions occur that defy such simple categorization. These collisions are thought to occur at smaller impact parameter where there is a lot of overlap of the projectile and target nucleus. They produce a spray of particles covering the forward hemisphere.[1,2,6] These particles are primarily nucleons and light nuclei with energies often exceeding 100 MeV/nucl[6] and an occasional nuclear fragment as heavy as oxygen with energies as high as 60 MeV/nucl.[7,8] Success at understanding this type of collision has been much more limited.

For intermediate bombarding energies, $250 \leq E \leq 400$ MeV/nucl, the proton spectrum above about 50 MeV/nucl can be qualitatively understood

in terms of a simple model[9,10] in which the geometrical overlap regions of the projectile and target fuse together and form a hot fireball source. Unfortunately, no other nuclei appear to be coming predominantly from this source.[8,11] This paper investigates the emission of high energy, $E \geq 200$ MeV, composite nuclei in relativistic nucleus-nucleus collisions. Data are presented on energy and angular distributions of nuclei produced in collisions of 500 MeV/nucl ^{40}Ar projectiles with Au target nuclei.[8] Nuclei with charges between 3 and 11 were observed. Inclusive spectra between 20 and 60 MeV/nucl and 35° to 85° were measured. These data are of particular interest because they are the only data for projectiles heavier than Ne and they cover an unusually wide range of fragments. Comparisons are made with similar data using lighter projectiles C, Ne.[7,8] For a brief account of this comparison see references 8 and 25.

In an attempt to interpret the data, thermal equilibrium, final state interaction and thermal-reaction equilibrium models of composite nucleus emission are considered. These models are shown to require parameter values that are far from those allowed by energy and momentum conservation. Two models are developed which involve thermal emission from a rotating or expanding spherical source. Neither of these models yields good quantitative fits to the data but they are a large improvement over energy and momentum conserving thermal models.

Although no satisfactory mechanism of composite nucleus emission is found, the data for all energies, angles and species may be simply parameterized. When the data points are transformed into a recoiling source frame with frame velocity $\beta_o = 0.08$ all data points lie near

($\pm 4x$) a common curve, for which the invariant cross section, $f \equiv \frac{1}{p} \frac{d^2\sigma}{d\Omega dE}$, falls exponentially with increasing momentum, $f \propto e^{-p/p_c}$, $p_c \simeq 340$ MeV/c.

Experimental Techniques

A. Exposure arrangement at the Bevalac

The experiment was carried out in a 48" long by 24" in diameter cylindrical vacuum chamber in Biomed Cave I at the Lawrence Berkeley Laboratory Bevalac.

A 50 μm thick Au target was placed in the center of the chamber and positioned at 45° to the beam axis. The detectors consisted of stacks of "Lexan" plastic charged particle detector sheets. Each stack consisted of 100 75 μm thick sheets, with a total thickness of .75 cm or .90 g/cm^2.

A total of 12 detector stacks covered the angular interval between 10° and 90°. The total solid angle of the detectors was 1.45 sr.

The 500 MeV/nucl ^{40}Ar beam was delivered in pulses of 1-2 x 10^7 particles per pulse for a total fluence of 1 x 10^{11} particles.

B. Lexan detector techniques

After the irradiation, sheets from the stacks were exposed to ultraviolet light and etched in 6.25 N NaOH at 40°C. This produces a visible etch pit or "track" along the path of a charged particle (with $Z \geq 3$) in the last few sheets before its end of range. The rate of track etching V_T of a fragment ^{A}Z, with charge Z, mass A and velocity βc is given by $V_T \propto (Z^*/\beta)^{\eta}$, where Z^* is the effective charge and $Z^* \leq Z$.[12] For ranges R of about 100 μm the range is roughly a power law in kinetic energy E, $R \propto E^{1.8}$ or $R \propto \beta^{3.6}$. Thus the rate of track etching V_T along the path of the particle at distances R from the end of range is approximately given by $V_T = K(Z,A)R^{-\alpha}$, where $\alpha \approx \eta/3.6$.

For R ≈ 100 μm and the standard UV exposure α equals 1.6. By measuring the etch rate at a known distance from the end of range it is possible to determine the charge and mass of the particle. In practice resolution of adjacent isotopes is difficult, and was not done in this experiment, although ^{8}Li was identified by its unique $^{8}Li \rightarrow {}^{8}Be \rightarrow 2\alpha$ decay and by a determination of its charge.

Since charge identification of a particle requires microscope measurement of each event it is impractical to measure and identify more than $\sim 10^{4}$ particles. Because of the observed fall-off of cross section with increasing charge most of the particles detected will have a charge near the lightest detectable charge. The solution to this problem is to vary the lightest detectable charge. The detection technique used in this experiment is to look for events that have etched a hole all the way through a sheet (Fig. 1), by passing anhydrous ammonia gas through them and onto ammonia-sensitive paper. For a fixed etch time there is a minimum charge for which this is possible. All lighter charged particles are not detected. Thus, by adjusting the etch time it is possible to set the minimum detectable charge. Not all particles above the charge threshold are in fact detected. The reason for this is that if a particle came to rest too deep into a given sheet the etch rates in the sheet just before that one will be too low to form a pair of connected cones. This is shown for the particle on the right in Fig. 1. Consider a particle coming to rest a distance ΔX below the surface of a sheet. Using eq. 1 the minimum etch time required to form a hole in the preceding sheet is given approximately by

$$t(\Delta X) = \frac{K}{(\alpha-1)}\left[[H+\Delta X]^{-(\alpha-1)} - [\Delta X]^{-(\alpha-1)}\right] \quad (1)$$

where H is the sheet thickness. If the etch time t_{etch} is less than $t(\Delta X)$ then no hole is formed and the particle is not detected. Thus there is a maximum distance below the surface $(\Delta X)_{max}$ that a particle can stop and still be detected. $(\Delta X)_{max}$ is given by $t((\Delta X)_{max}) = t_{etch}$. Assuming that for all particles, detected or not, ΔX is uniformly distributed between zero and H, then the detection efficiency P equals $P = \frac{(\Delta X)_{max}}{H}$. The detection efficiency as a function of etch time, and charge, calculated in this manner, is shown in Fig. 2. The actual $(\Delta X)_{max}$ used in cross section calculations was determined from a distribution of measured values of ΔX.

Etch times of 50, 30 and 10 hours were used. The corresponding charge thresholds as shown in Fig. 2 were 4, 5 and 7 respectively. Figure 3 shows a plot of etch rate vs. range for 500 events from the 30 hr etch. Due to the spread of ranges and the relatively small number of higher charged events the charge resolution is not very striking. Since the range dependence of the etch rate is known $V_T \propto R^{-1.6}$ it is possible to adjust the etch rate for range differences and compare etch rates at a common range. Thus it is useful to define the range adjusted etch rate, $V_T(@100\ \mu m) = V_T(R)(R/100\ \mu m)^{1.6}$, which is the measured etch rate corrected to a common range of 100 μm. Figure 4 shows histograms of number of events vs. range adjusted etch rate, $V_T(@100\ \mu m)$, for the three different etch times. Individual charge peaks are observed. The charge assignments are based on measurements, shown in Fig. 4, of ^{8}Li and ^{8}B nuclei which are identified by their

2α decay. The final histogram in Fig. 4 in which charges 9-11 were detected used a slightly different processing scheme, 1/4 the normal UV dose and a 20 hr etch. Reducing the UV dose had the effect of shifting the sensitivity down so that only particles with $Z \geq 9$ would be detected. This avoided the use of a very short etch time for which the ammonia detection scheme is unreliable. The 10 and 50 hr etches were cross checked with the 30 hr etch where the absolute ^{8}Li, ^{8}B charge calibrations was available. The 1/4 normal UV dose and 20 hr etch data was cross calibrated with the 50 hr etch.

The ^{8}Li data were obtained by microscopic scanning for tracks that end with the characteristic 2α decay of ^{8}Li. The contribution of background ^{8}B, which can be distinguished from ^{8}Li by its higher etch rate, has been found to be negligible.

Experimental Results

A complete list of all the measured cross sections is given in Table 1. Cross sections at selected angles are plotted in Fig. 5a,b, c as a function of kinetic energy/nucleon.

The cross sections shown in Fig. 5a,b,c display a number of common features. They fall monotonically with increasing energy/ nucleon and angle. The energy spectra fall approximately exponentially with increasing energy/nucleon. The slopes of the energy spectra steepen with increasing mass. The cross sections at fixed angle and energy per nucleon fall off with increasing fragment mass, about a factor of 10^3 between ^{6}Li and Na.

Figure 6 shows the energy spectrum at 55° for each species. The abscissa in this case is total kinetic energy rather than energy per nucleon. Several regularities appear when the data are plotted in this way. Unlike Fig. 5a,b,c, the slopes of the energy spectra are roughly independent of fragment size. Also the cross section falls much more slowly with increasing fragment size, only about a factor of 10 between B and Na.

The fact that the spectra for the different species have similar slopes and magnitudes when plotted as a function of total kinetic energy suggests that total kinetic energy is perhaps a more relevant variable than kinetic energy per nucleon.

The angular distributions, although not the same for all species, show no systematic dependence on fragment size. A typical set of angular distributions, for B, is shown in Fig. 7. Typically the angular distributions are flat at small angles and steepen somewhat beyond 60°.

Figure 8 shows the data from a similar experiment,[8] 400 MeV/nucl $^{20}Ne + U \rightarrow X$, where ^{8}Li, B and C fragments were measured. The cross sections have similar energy and angular dependences. The primary difference is that the cross sections with ^{20}Ne projectiles are about a factor of 4 smaller than those with ^{40}Ar projectiles. Although the beam energy/nucleon and target are not identical in the two experiments, they are similar enough to suggest that the increase in cross sections in this experiment is primarily due to the doubling of the projectile mass.

Several key features of the data are worth noting:

1. Fragment spectra are smooth and fall monotonically with increasing energy and angle.

2. The spectra fall approximately exponentially with increasing energy.

3. The slopes of the energy spectra are roughly independent of fragment size when plotted as a function of the total kinetic energy rather than kinetic energy per nucleon.

4. Fragment cross sections fall off much more slowly with increasing fragment size, when compared at the same total kinetic energy rather than kinetic energy per nucleon.

5. Fragment cross sections are about a factor of 4 higher with 500 MeV/nucl ^{40}Ar projectiles than with ^{20}Ne projectiles of comparable energy per nucleon.

Summary of Existing Models

A. Models of composite nucleus emission in relativistic proton nucleus collisions

Before relativistic heavy ion data became available, several useful models had already been developed to explain certain features of composite nucleus emission in relativistic proton-nucleus collisions.

Evaporation models envisioned composite nuclei thermally boiling off the surface of a recoiling excited target nucleus.[13,14] These models were used to fit the energy spectrum at one angle for nuclei with energies $E \lesssim 100$ MeV. Agreement with the angular distribution was not good. Typical parameters for 5 GeV protons on a uranium target are temperatures $\tau \approx 12$ MeV and recoil velocities $\beta_o \equiv v_o/c \approx 0.006$.[14] Theoretical attempts to explain these parameters reached the conclusion that the temperatures were unexplainably high.[14] Another difficulty with this model was that the tails of the energy spectra were too high and flat, being characterized by "local" temperatures of about 20 MeV. No attempt was made to explain the absolute or relative yields of the fragments.

A second model was developed by Butler and Pearson[15] to explain the emission of relativistic deuterons in 25-30 GeV proton-nucleus collisions. Their model was that, if they had sufficiently similar momenta, nucleons in the nuclear cascade could coalesce to form deuterons by interacting with the residual nucleus as a third body. Both of these models have been modified and adapted to explain composite nucleus emission in relativistic heavy ion collisions.[10,16]

B. The "Fireball" model of proton emission in relativistic heavy ion collisions.

A number of different models have been developed to explain proton emission in relativistic heavy ion collisions. They include analytic and numerical hydrodynamic calculations and Monte-Carlo cascade calculations,[17-23] both of which attempt to follow the detailed time evolution of the collision.

The "Fireball" model developed by Westfall et al.[9] is perhaps the most successful and certainly the simplest model of proton emission. The model treats both target and projectile as spheres with nucleons distributed uniformly throughout their volume. In a classical picture as two spheres graze each other they form clean, cylinder-like cuts in each other. In the "Fireball" model the nucleons in these cylinders mix together and thermally equilibrate to form the fireball. The hot recoiling fireball then completely boils away to form the observed nucleons. At a given impact parameter the fireball can be characterized by the number of nucleons, recoil velocity and temperature, all of which can be calculated from geometry and energy and momentum conservation. The calculated cross sections, for beam energies, $E \lesssim 400$ MeV/nucl, are generally within a factor of two or less of the measured cross sections and have roughly the right slopes of energy and angular distributions. Data for 2.1 GeV/nucl ^{20}Ne + U are much more isotropic than predicted by the "Fireball" model and the absolute magnitudes are not predicted well. These shortcomings are perhaps partly due to the target failing to stop the projectile at such high energies. The success of this model in predicting proton cross sections suggests that it would be a good starting point for coalescence-type calculations of composite nucleus emission.

C. Final state interaction model of composite nucleus emission in relativistic heavy ion collisions

The final state interaction or coalescence model of Butler and Pearson[15] was extended by Gutbrod et al.[16] to explain emission of composite nuclei in relativistic heavy ion collisions. In the model of Gutbrod et al., if Z protons and N neutrons all had momentum vectors differing by less than a coalescence radius p_o these nucleons would form a nucleus $^{(N+Z)}A$ provided it corresponded to a bound nucleus. Thus, given the nucleon differential cross section the cross section for a nucleus of mass A is given by

$$\frac{d^2\sigma_A}{p^2dpd\Omega} = \frac{1}{A!}\left(\frac{4\pi p_o{}^3\gamma}{3\sigma_o}\right)^{A-1}\left(\frac{d^2\sigma_1}{p^2dpd\Omega}\right)^A . \qquad (2)$$

Cross sections σ_A and σ_1 are nucleus and nucleon cross sections respectively and are evaluated at the same momentum per nucleon with Lorentz factor γ. σ_o is the total reaction cross section. The coalescence radius p_o is the only adjustable parameter.

This model successfully accounted for the systematic increase in slope of energy spectra with increasing mass when plotted as a function of energy per nucleon. It satisfactorily fit cross sections for production of H and He isotopes with p_o values of about 100 MeV/c, on the order of the Fermi momentum of light nuclei.

In spite of this success there are several difficulties and inconsistencies within the model:

1. There is no requirement that the nucleons be spatially close enough to become bound.

2. Spin and isospin statistics are not taken into account. This

is not really a serious problem for H and He isotopes, which have only ground states, but becomes important for heavier nuclei which have a large number of excited states.

3. Since eq. 2 is very nonlinear in the nucleon cross section, using a nucleon cross section that is an average over many collisions is incorrect, particularly since the multiplicity is known to vary enormously from event to event.

4. Since the nucleon spectrum is depleted significantly by the formation of nuclei in this model the nucleon spectrum in eq. 2 is not the observed nucleon spectrum but is rather a "primordial" spectrum including all nucleons emitted in nuclei.

D. Reaction equilibrium model of composite nucleus emission in relativistic heavy ion collisions

Mekjian[24] adapted the formalism previously used to explain atomic and nuclear reaction equilibria in stars to explain the production of composite nuclei in relativistic heavy ion collisions. Mekjian assumed that after the fireball of Westfall et al. was formed, nuclear reactions among the nucleons would occur that would form composite nuclei within the fireball. Consider a volume V_o in equilibrium at a temperature T_o. The number of nuclei contained within the volume $N_o(Z,N)$ of type $(Z+N)_Z$ is given by

$$N_o(Z,N) = \left(\frac{[\lambda(T_o)]^3}{V_o}\right)^{A-1} \frac{f(Z,N)}{2^A} (N_o(1,0))^Z (N_o[0,1])^N , \qquad (3)$$

where $\lambda(T_o) = hc(2\pi m_p c^2 kT_o)^{-\frac{1}{2}}$, $A = Z + N$ and $N_o(1,0)$, $N(0,1)$ are the number of protons and neutrons in the volume V_o respectively, and

$$f(Z,N) = A^{3/2} \exp(E_o(Z,N)/kT_o) \sum_j (2S_j+1) \exp(-E_j/kT_o) \quad . \qquad (4)$$

E_o is the ground state energy of the nucleus and E_j and S_j are the excitation energies and spins of states of the nucleus. The sum extends over all states of the nucleus.

This establishes the relative yields of composite nuclei as a function of the density of neutrons and protons. The relationship between the proton and composite nucleus cross sections then becomes

$$\frac{d^2\sigma(Z,N)}{dEd\Omega} \propto \left[\frac{d^2\sigma(1,0)}{dEd\Omega}\right]^A \quad . \qquad (5)$$

The functional form of the result is in fact exactly the same as with the final state interaction model.

The most serious difficulty with this model is that it assumes that reaction equilibrium has time to occur. Rough calculations indicate that a nucleon might suffer ~10 or fewer collisions[22] before the fireball system breaks up. Even for deuterons to be in reaction equilibrium would require a major portion, more than 20%, of the n + p cross section to be n + p + nucleus → d + nucleus*.

The most important feature of this model is that it demonstrates that, for thermal nucleon spectra, the coalescence model is equivalent in form to the simple assumption of thermal equilibrium between composite nuclei and nucleons. Thus, if the proton spectrum can be characterized as being emitted from a recoiling source with source velocity $\beta_o c$ and source temperature τ, both the coalescence and reaction equilibrium models predict the same results, namely that composite nuclei can be characterized by the same source velocity $\beta_o c$ and source

temperature τ. This may be simply shown from eq. 5. A thermal nucleon source viewed in the source (primed) frame has a proton cross section given by $\frac{d^2\sigma(1,0)}{d\Omega' dE'} \propto \exp(-E'/\tau)$. From eq. 5 the cross section from mass A fragments in the same frame is $\frac{d^2\sigma(Z,N)}{d\Omega' dE'} \propto [\exp(-E'/\tau)]^A = \exp(-AE'/\tau)$. AE' is the total kinetic energy of the mass A fragment. So mass A fragments are isotropic and thermal when viewed in the source frame of the nucleons. Thus, composite nuclei have the same source velocity and source temperature as nucleons in both the coalescence and nuclear reaction equilibrium models.

Comparison of Models with the Data

Since no measurements exist of inclusive proton cross sections in Ar + Au collisions, tests of the coalescence and reaction equilibrium models of composite nuclei must be indirect. If composite nuclei are emitted from a blob of nucleons recoiling with source velocity $\beta_o c$ and in thermal equilibrium at source temperature τ then both models predict that all composite nuclei should be characterized by the same source velocity and source temperature. All species can be individually fit by such a model, but not all by a common value of β_o and τ. For the fits the cross section is given by $\frac{d^2\sigma}{d\Omega dE} = K \frac{P}{P'} \sqrt{E'} e^{-E'/\tau}$ where P' and E' are the momentum and total kinetic energy of the fragment in the source frame which has a source velocity β_o and P and E are the same quantities in the laboratory frame. In each case a good fit was obtained when the one standard deviation error of the cross section was taken to be given by counting statistics plus 5% of the cross section. Figure 9 shows in β_o-τ space 90% confidence level contours of the value of β_o and τ for each species. Although there is a general clustering around $\beta_o \approx 0.08$ and $\tau \approx 60$ MeV, there is very little overlap of the contours. Thus the reaction equilibrium model does not fit the data and neither does the coalescence model if one assumes thermal nucleon spectra.

A more serious difficulty than the lack of agreement on a common value of β_o and τ is the problem of explaining the generally low β_o and high τ. First consider the composite nuclei to be emitted from a hot recoiling blob of nuclear matter formed by N_p projectile nucleons inelastically colliding with N_T target nucleons. There is a unique relation between β_o and τ shown in Fig. 10 that is determined by energy

and momentum conservation only. The high and low β_o ends of the curve correspond to mixtures consisting primarily of projectile and target nucleons respectively. If one considers partially elastic collisions the projectile and target nucleons form separate blobs. The open curve in Fig. 10 is for 50% elasticity, the low β_o branch is the target nucleon blob. The rectangular box at low β_o in Fig. 10 contains all the 90% confidence contours of the data. Most of the mixing curve lies at values of β_o much higher than the data box. Figure 11 shows the individual confidence level contours of Fig. 9 with the mixing curves superimposed. Note that no contour intersects the curves. Points on the mixing curve with roughly the right values of β_o have temperatures a factor of 3 to 4 too low. Gosset et al.[10] have found that thermal fits to B spectra from 400 MeV/nucl Ne + U yield temperatures a factor of two higher than expected. They suggest that this discrepancy may be explained by the fact that formation of composite nuclei in the blob should raise the temperature of the system by reducing the number of particles. However, in order to raise the temperature by a factor of 4 the average mass of incipient fragments in the blob, including nucleons, would have to be 4 m_p, that is four nucleon masses. In the case of 400 MeV/nucl ^{20}Ne + U where light fragment data are available it is known that nucleons are the dominant species emitted and that alpha particle yields are more than an order of magnitude lower.[10] Thus, this mechanism cannot be the primary cause of the temperature discrepancy.

A more direct test of the coalescence model is to check if any proton spectrum of arbitrary form can correctly generate the spectra for all species. Equation 2 may be used to calculate an unknown

proton spectrum based on a known composite nucleus spectrum, although it is normally used to do the reverse calculation. Since the coalescence formula contains an adjustable normalization parameter p_o it is not possible to calculate the magnitude of the proton cross sections required to fit a given composite nucleus spectrum, but it is possible to calculate the shapes of the proton spectra. Figure 12 shows the proton spectrum required to fit the Ne fragment data. Below it are the measured proton spectra of Westfall et al.[10] for 250 and 400 MeV/nucl ^{20}Ne + U. Note that the calculated proton spectrum is qualitatively quite different from either measured proton spectrum. The calculated spectrum rises slowly with increasing energy and is nearly isotropic, in the laboratory frame. The slow variation with energy and angle is because $\frac{d^2\sigma}{d\Omega dE}|_{proton} \propto \left[\frac{d^2\sigma}{d\Omega dE}|_{Ne}\right]^{(1/A_{Ne})}$, thus the calculated proton spectrum varies as the 20th root of the Ne spectrum, taking Ne to be ^{20}Ne. A factor of 10 difference in cross section between two points at the same energy and different angles in the Ne spectrum results in a 12% difference in cross section in the corresponding proton points. With the calculated proton spectrum it is possible to calculate the shape of all other composite nucleus spectra. Figure 13 shows the calculated boron spectrum and compares it with the data. The calculated boron spectrum falls off more slowly with increasing energy and angle than the data. The differences are not as striking as for the calculated proton spectrum, because $\frac{d^2\sigma}{d\Omega dE}|_B \propto \left[\frac{d^2\sigma}{d\Omega dE}|_{Ne}\right]^{(A_{boron}/A_{neon})}$, and the masses of boron and neon are comparable.

Two conclusions can be drawn: (1) Although the spectra of composite nuclei can be qualitatively fit by thermal models, the values

of the parameters needed are in gross disagreement with energy and momentum conservation. (2) Although the coalescence model can crudely fit the observed composite nucleus spectra, the required proton spectrum is quite different from measured spectra for similar reactions. The required proton spectrum, if parameterized in terms of a thermal model, is also in gross disagreement with energy and momentum conservation.

It hardly seems surprising that emission of composite nuclei containing 10-20 nucleons cannot be explained by the reaction equilibrium or coalescence models. It would be very hard to understand how such processes could occur for all but the lightest composite nuclei. The failure of thermal models to explain the data suggests that other means of energy transfer to composite nuclei should be considered.

Non-thermal Models of Composite Nucleus Emission

The difficulty with thermal models, as discussed in the previous section, is that the parameters required to fit the data have a low value of $\beta_o \simeq 0.08$ and a high temperature $\tau \simeq 60$ MeV, which is incompatible with energy and momentum conservation. The root of the difficulty with thermal models is that they require all species, including nucleons, to have total kinetic energy spectra in the source frame that differ only by constant factors.

This section will explore mechanisms that preferentially give the energy of a system to the higher mass fragments. The models are all based on the same idea, that if moving matter breaks up, each piece is given energy in proportion to its mass. In other words, the velocity of the emitted fragment is the relevant quantity, not its kinetic energy or momentum.

A. Spinning, exploding target

The first model to be considered is based on the process called "target explosion" by Westfall et al.[9] They assumed that at sufficiently small impact parameter, the entire projectile might stop in the target and form a large, hot recoiling system of nucleons. Westfall et al. suggested that this process might explain the discrepancies between the fireball model and measured proton spectra at low energies, $E \lesssim 80$ MeV. For 500 MeV/nucl ^{40}Ar + Au the velocity and temperature are $\beta_o = 0.18$ and $\tau = 40$ MeV. If this process occurs at non-zero impact parameters, the angular momentum of the system is non-negligible, that is, a significant fraction of the center of mass energy is rotational energy. My modification of the target explosion model is to assume that it occurs in non-zero impact parameter collisions and is the

principal source of composite nuclei. Specifically, my model takes the projectile, target, and composite exploding system to be spheres of radius $R = 1.2\ fm(A)^{1/3}$. It assumes that the explosion process occurs for all impact parameters b such that the projectile is completely engulfed within the target, i.e., $b \leq (R_T - R_P)$, where R_T and R_P are the target and projectile radii.

The calculation I have done is a Monte Carlo routine that proceeds by the following steps:

1. Pick a point of impact from which an angular velocity and axis of rotation are calculated.

2. Calculate the angular momentum of the system and its temperature. The temperature is a function of impact parameter because the rotational energy is, and the thermal energy plus rotational energy must equal the constant center of mass energy.

3. Pick a "point of departure" for the composite nucleus randomly out of the entire volume of the "target explosion" sphere. Pick a thermal energy and direction of motion measured in the local rest frame of the medium.

4. Transform the particle first out of the rotating medium into the center of mass frame of the "target explosion" system and then finally into the laboratory frame.

The results of this calculation are shown for oxygen in Fig. 14 and compared with the data in the same figure. The model is unsatisfactory, predicting much too rapid a fall-off with increasing angle. Further, it leads to a turnup in the backward direction at low energies, $E \leq 10$ MeV/nucl, that could be tested experimentally. Later I will consider a modified version of this model.

B. Expanding target explosion

Bondorf et al.[21] noted that the fireball of Westfall et al.[9] would expand and cool after formation, converting thermal energy to energy associated with a velocity of expansion. They solved the problem of an expanding gas sphere in a vacuum and analytically did the transformations and averages to calculate a laboratory cross section. Although their calculations were for emission of nucleons, it is possible to extend the calculation to the emission of composite nuclei. It is necessary, however, to make the following assumptions:

1. That the concentration of composite nuclei in the nucleon gas is sufficiently small that it does not alter the behavior of the nucleon gas.

2. That the ratio of density of composite nuclei to density of nucleons is independent of position.

3. That the composite nuclei flow with the expanding nucleon gas and are in local thermal equilibrium with the gas.

Figure 15 shows the calculated energy spectrum for oxygen for $\alpha = \frac{1}{2}$. α is the one free parameter of the model which determines the radial distribution of the gas. The radial distribution is given by $\rho(r) = \frac{A}{R^3}\left[1-\left(\frac{r}{R}\right)^2\right]^{\alpha}$ where r is the distance from the center of the sphere, R is the radius of the sphere and A is a constant fixed by the number of particles in the system. The distribution is very isotropic and has a rising energy spectrum, not at all like the data. The isotropy and rising cross section are also features of the calculated nucleon spectra at low energies. Varying the parameter α between 0 and 10, covering the complete range Bondorf and co-workers believe to be physically reasonable, does not alter the basic discrepancies with the

data.

It is possible, however, to introduce several, more sensitive, free parameters into the calculation. Bondorf et al. assume that the coupling of thermal energy to energy of expansion stops when the expansion velocity equals the "thermal velocity." The time at which this occurs is called the time at breakup, t_b. Once breakup occurs the energy and angular distributions of nucleons are fixed. In the calculation of oxygen spectra for Fig. 15 it was assumed that they remained coupled to the nucleon gas until time t_b was reached. It is possible that composite nuclei decouple from the nucleon gas at a time, $t_d \leq t_b$ before the nucleon gas breaks up. It is also possible that the collision is not completely inelastic, that is, the elasticity $\varepsilon > 0$ and the projectile and target separate after the collision. Figure 16 show the results for $t_d = 0.5\ t_b$, $\varepsilon = 0.3$ and $\alpha = 10$, which is χ^2 minimizing best fit to the data for $\alpha \leq 10$. χ^2 does not appear to have a minimum as a function of α for $\alpha \leq 100$, however, χ^2 only drops by about 1% between $\alpha = 10$ and $\alpha = 100$. This calculation gives curves that fit the data much better than the previous one. The angular distribution is less isotropic and the energy spectrum falls with increasing energy. Unfortunately the flatness of the energy spectrum at low energies is in systematic disagreement with the data.

One possible difficulty with both of these non-thermal models is that they assume that the elasticity of the collision is constant, independent of impact parameter. In order to calculate the elasticity as a function of impact parameter it is necessary to know how much momentum a projectile nucleon loses as it passes through a thickness T of target nuclear matter. Sobel et al.[20] suggest that the final

momentum of the projectile nucleon is given approximately by $P = P_o \exp(-T/T_p)$. P_o and P are the initial and final momenta of the projectile nucleon in the collision center of mass frame. T_p is the momentum transfer length which is about 2.5 Fermis for beam energies 300 MeV/nucl < E_{beam} < 600 MeV/nucl. The elasticity can be calculated using this formula and taking the naive assumption that the projectile may be treated as independent nucleons passing through an undeformed target nucleus. The result of this calculation is shown in the top of Fig. 17a for 500 MeV/nucl ^{40}Ar + Au. Note that the elasticity is substantially greater than zero over a fairly wide range of impact parameters. The remaining parts of Fig. 17 show the target recoil β, the target internal energy per nucleon, and the target angular momentum as a function of impact parameter for 500 MeV/nucl ^{40}Ar + Au. Using these values of kinematic variables, I have recalculated the results of the spinning and expanding target explosion models. Figure 18 shows these results for oxygen fragments, for which an average was done over all impact parameters. In the case of the expanding target explosion model the parameters α and t_d were calculated to best fit the data and have values α = 10, $t_d = 0.4\ t_b$. The upper two graphs of Fig. 18 show for comparison the oxygen calculation using the thermal model, for which the collision was assumed to be central and completely inelastic, and also an impact-parameter-averaged thermal model with parameter values given in Fig. 17a,b. The oxygen data are superimposed on each figure. Clearly none of the models represents the data well. The angular distributions are substantially too steep in each case. The thermal models are by far the worst. The steepness of the angular distribution is due to the high recoil velocity of the target in central

collisions. It is possible that the most central collisions are so violent that they do not produce large fragments such as oxygen. In any case, it is interesting to see what happens when small impact parameters are excluded. Figure 19 shows the same calculations as Fig. 18 except that the most central 20% of the cross section has been excluded. The results are considerably better than before for the nonthermal models. They are more nearly isotropic, in agreement with the data. The expanding target explosion model appears to give the best fit to the data, but it still has a systematic flattening at low energies that is uncharacteristic of the data.

The fraction of cross section excluded, 20%, was chosen arbitrarily. It may be possible to achieve good quantitative fits to the data with the expanding target explosion model by carefully adjusting the limiting impact parameter within which central collisions are to be excluded, along with the other adjustable parameters α and t_d. To achieve a good fit with several adjustable parameters would not be too surprising. I believe it is highly significant, however, that much better representations of the data can be obtained with simple nonthermal models involving expansion or rotation processes than with purely thermal processes.

A model for fragment production that treats the coupling between thermal energy, expansion energy, and energy of rotation may be necessary. This might be possible to do with a Monte Carlo routine or may require a full hydrodynamic calculation similar to those already used to predict proton spectra.

A Universal Curve of Invariant Cross Section vs. Momentum

Although no model has been found to fully describe the data, the data do show some surprising regularities. For example, as mentioned previously, the slopes and magnitudes of energy spectra appear much more comparable when comparing different species if the cross sections are plotted vs. total kinetic energy rather than energy per nucleon. There are other ways of plotting the data that make this result more striking. An important step in looking for regularities in the data is to eliminate the distortion associated with emission from a recoiling source. This can be crudely done by transforming back into an average source frame with velocity $\beta_o \simeq 0.08$. For convenience in doing transformations it is easier to use the Lorentz-invariant cross section $f \equiv (1/p)d^2\sigma/d\Omega dE$ rather than the laboratory cross section.

Figure 20 shows the invariant cross section plotted vs. the momentum p' in the recoiling frame with $\beta = 0.08$. The data for both 400 MeV/nucl ^{20}Ne + U and 500 MeV/nucl ^{40}Ar + Au reactions show similar features. In both reactions all data points fall on a straight line within a factor of about ±4 or less, thus corresponding to an exponential fall-off with momentum.[25] It seems surprising that over 200 data points, in the case of ^{40}Ar data, at all energies, lab angles, and for all species from Li to Na, which vary by a factor of $\sim 10^6$ in invariant cross section, would fall so close to a common line. It is interesting that the slopes of the curves for the two reactions are not the same. The ^{40}Ar curve is flatter. The characteristic or e-folding momentum for the ^{20}Ne reaction is $P_c \simeq 230$ MeV/c and for the ^{40}Ar reaction is $P_c \simeq 340$ MeV/c.

The transformation of the data for all species into a common frame

is a reasonable first step but can be refined considerably. A more useful technique for studying the energy or momentum dependence of the invariant cross section is to calculate the value of the laboratory momentum for a fixed value of the invariant cross section. A plot of points of constant invariant cross section on a graph of transverse momentum $p_\perp$ vs. longitudinal momentum $p_{||}$ should lie on a circle if emission is isotropic from sources with a single velocity. Actually this is only true in the nonrelativistic limit. The circles become ellipses when relativistic calculations are done. However, in the case of the data presented here ellipse eccentricities e never exceed e = 0.01 and this refinement may be neglected. Figures 21a,b,c are plots of this type in momentum space for the data presented here. The points do fall quite well on circles as demonstrated by the "eyeball" circles drawn through them. From the displacements of the circles along the $p_{||}$ axis the velocity of the "source" may be calculated. An important observation can be made from these plots, that the "source" velocity increases with increasing fragment momentum or decreasing invariant cross section. This is even more clearly demonstrated in the analysis of ref. 8 of 400 MeV/nucl ^{20}Ne + U data. The roughly uniform increase in momentum radius with each ~3 fold decrease in cross section graphically demonstrates the exponential dependence of cross section on the momentum in the source frame p'. The approximate constancy of radius for a given invariant cross section, independent of fragment mass, demonstrates that the invariant cross sections for all species lie near a common universal curve.

It is now possible to plot the invariant cross section vs. p' independent of any simplifying assumptions about the source recoil

velocity. Figure 22 shows such plots for the 500 MeV/nucl ^{40}Ar + Au and 400 MeV/nucl ^{20}Ne + U data and also for previous 2.1 GeV/nucl ^{12}C + Au data.[25] The abscissa is the source velocity determined graphically. The data for ^{40}Ar and ^{20}Ne look much like those in Fig. 20. The ^{12}C and ^{20}Ne data have very similar slope and magnitude. Perhaps the differences in mass and energy per nucleon tend to compensate for each other.

The simplicity of this result seems to suggest that an equally simple model should account for the basic features of the data: low source velocity, exponential fall-off of the cross section with either total energy or momentum, and similar values of invariant cross sections from species to species evaluated at the same momentum in the source frame. Certainly any model that attempts to explain the yields of composite nuclei must naturally account for the very slow fall-off of cross section with increasing fragment mass when compared at the same total momentum.

Summary and Conclusion

I have presented data on the emission of composite nuclei in collisions of 500 MeV/nucl ^{40}Ar + Au and attempted to explain it in terms of five different models. The first three models, thermal, final state interaction, and reaction equilibrium, have been developed by others and applied to previous data. The fourth model of a spinning target explosion was developed in this paper. The fifth model of an expanding, exploding target, which was previously developed to explain proton emission, was modified in this paper to explain composite nucleus emission. None of these models provided quantitative fits to the data without introducing free parameters.

The thermal and reaction equilibrium models are the same regarding their predictions of the shapes of energy and angular distributions of composite nuclei. The distributions should be isotropic Maxwellian distributions when transformed back into some recoiling source frame. Although good fits of each species individually are obtained with the thermal model, the values of the source recoil velocity β_o and temperature τ obtained are not consistent with being the same for all species. A more serious difficulty is that all the values of β_o and τ are inconsistent with rather simple energy and momentum conservation considerations. Typically values of τ are about a factor of four higher than expected for the value of β_o obtained.

A direct test of the final state interaction model would require a knowledge of the as yet unmeasured proton cross sections for 500 MeV/nucl ^{40}Ar + Au. However, by assuming the model is correct, it is possible to use composite nucleus spectra to calculate the shape of the proton spectrum or other composite nucleus spectra. The shape

of the proton spectrum calculated from the Ne fragment data is qualitatively different from any measured proton cross section for relativistic heavy ion collisions. The shape of the boron cross section based on the neon spectrum falls more slowly with increasing energy and angle than the data. This result is typical of those obtained with other pairs of species, namely, that proton spectra based on high mass fragments give energy and angular distributions for lighter species that are significantly too flat. Thus, although the final state interaction model may explain the emission of composite nuclei as heavy as alpha particles, it does not seem to work for the heavier composite nuclei.

Neither the spinning nor the expanding target explosion model in simplest form offers adequate fits to the data. However, a modified form of the expanding target explosion model seems promising since this model fits the data much better than thermal models that are required to be energy and momentum conserving. It seems likely that a correct accounting of the connection between expansion, rotation, and cooling would be necessary to make the target explosion model viable. Since such a calculation would be quite complicated and would require many simplifying approximations a hydrodynamic calculation might be a better approach.

Despite the failure of these models the data demonstrate striking regularities. All fragments appear to be isotropically emitted in a recoiling source frame. The invariant cross sections viewed in the source frame fall exponentially with fragment momentum in the source frame P'. The invariant cross sections have no obvious fragment mass dependence when compared at the same P'.

It seems likely that an explanation of the anomalous flatness of the energy spectra of composite nuclei will involve models with a combination of acceleration mechanisms such as thermal, expansion, and rotation. If this is so, then information on the emission of large composite nuclei will be most helpful in revealing the nonthermal acceleration mechanisms.

References

1. H.H. Heckman, D.E. Greiner, P.J. Lindstrom, and D.D. Tuttle, "An Atlas of Heavy Ion Fragmentation Topology," LBL preprint (1976), unpublished.

2. R. Poe, S. Fung, B. Gorn, A. Kernan, G. Kiernan, J. Lee, J. Ozawa B. Shen, G. Van Dalin, L. Schroeder, and H. Steiner, to be published.

3. D.E. Greiner, P.J. Lindstrom, H.H. Heckman, B. Cork, and F.S. Bieser, Phys. Rev. Lett. 35, 152 (1975).

4. P.J. Lindstrom, D.E. Greiner, H.H. Heckman, B. Cork, and F.S. Bieser, LBL preprint 3650 (1975).

5. J. Papp, J. Jaros, L. Schroeder, J. Staples, H. Steiner, A. Wagner, and J. Wiss, Phys. Rev. Lett. 34, 601 (1975), and to be published.

6. A.M. Poskanzer, R.G. Sextro, A.M. Zebelman, H.H. Gutbrod, A. Sandoval, and R. Stock, Phys. Rev. Lett. 35, 1701 (1975).

7. H.J. Crawford, P.B. Price, J. Stevenson, and L.W. Wilson, Phys. Rev. Lett. 34, 329 (1975).

8. J. Stevenson, P.B. Price, and K. Frankel, Phys. Rev. Lett. 38, 1125 (1977).

9. G.D. Westfall, J. Gosset, P.J. Johnsen, A.M. Poskanzer, W.G. Meyer, H.H. Gutbrod, A. Sandoval, and R. Stock, Phys. Rev. Lett. 37, 1202 (1976).

10. J. Gosset, H.H. Gutbrod, W.G. Meyer, A.M. Poskanzer, A. Sandoval, R. Stock, and G.D. Westfall, LBL preprint 5820 (1977).

11. S. Garpman, J.P. Bond, and P.J. Siemens, to be published.

12. Robert L. Fleischer, P. Buford Price, and Robert M. Walker, Nuclear Tracks in Solids: Principles and Applications, University of California Press (1975).

13. V. Weisskopf, Phys. Rev. 52, 295 (1937).

14. A.M. Poskanzer, G.W. Butler, and E.H. Hyde, Phys. Rev. C3, 882 (1971).

15. S.T. Butler and C.A. Pearson, Phys. Rev. Lett. 7, 69 (1961), and Phys. Rev. 129, 836 (1963).

16. H.H. Gutbrod, A. Sandoval, P.J. Johansen, A.M. Poskanzer, J. Gosset, W.G. Meyer, G.D. Westfall, and R. Stock, Phys. Rev. Lett. 37, 667 (1976).

17. G.F. Chapline, M.H. Johnson, E. Teller, and M.S. Weiss, Phys. Rev. D8, 4302 (1973).

18. H.G. Baumgardt, T.U. Schott, Y. Sakamoto, E. Schopper, H. Stöcker, J. Hofmann, W. Scheid, and W. Greiner, Z. Phys. A273, 359 (1975).

19. A.A. Amsden, G.F. Bertsch, F.H. Harlow, and J.R. Nix, Phys. Rev. Lett. 35, 905 (1975), and to be published.

20. M.I. Sobel, P.J. Siemens, J.P. Bondorf, and H.A. Bethe, Nucl. Phys. A251, 502 (1975).

21. J.P. Bondorf, S. Garpman, E.C. Halbert, and P.J. Siemens, to be published (1976).

22. A.A. Amsden, J.N. Ginocchio, F.H. Harlow, J.R. Nix, M. Danos, E.C. Halbert, and R.K. Smith, Los Alamos preprint LA-UR-77-152, (1977), to be published.

23. A.R. Bodmer and C.N. Panos, Phys. Rev. C15, 1342 (1977).

24. A. Mekjian, Phys. Rev. Lett. 38, 640 (1977).

25. P.B. Price, J. Stevenson, and K. Frankel, Phys. Rev. Lett. 39, 177 (1977).

Table Captions

Table 1. A complete list of the data presented in this paper. E+ and E- define the upper and lower limits of the energy interval over which the cross section was averaged. $\sigma+$ and $\sigma-$ are 68% confidence limits on the cross section.

TABLE 1.

Species	Angle θ (deg)	±Δθ† (deg)	Energy E (MeV/nucl)	E+† (MeV/nucl)	E- (MeV/nucl)	Cross Section σ (μb/MeV-sr)	σ+† (μb/MeV-sr)	σ- (μb/MeV-sr)
^{8}Li	40	2	8.0	9.6	6.7	1.85×10^{2}	2.49×10^{2}	1.36×10^{2}
^{8}Li	40	2	11.4	12.7	10.3	1.42×10^{2}	1.96×10^{2}	1.06×10^{2}
^{8}Li	40	2	13.6	14.6	12.3	1.91×10^{2}	2.68×10^{2}	1.34×10^{2}
^{8}Li	40	2	30.3	31.2	29.5	3.10×10^{1}	4.52×10^{1}	2.09×10^{1}
^{8}Li	60	2	8.0	9.9	6.7	1.68×10^{2}	2.12×10^{2}	1.33×10^{2}
^{8}Li	60	2	11.4	12.9	10.3	1.11×10^{2}	1.58×10^{2}	7.66×10^{1}
^{8}Li	60	2	13.6	14.8	12.3	7.70×10^{1}	1.06×10^{2}	5.51×10^{1}
^{8}Li	60	2	19.9	21.0	19.0	5.20×10^{1}	7.76×10^{1}	3.40×10^{1}
^{8}Li	80	2	8.2	10.2	6.0	1.36×10^{2}	1.98×10^{2}	9.15×10^{1}
^{8}Li	80	2	12.6	14.3	11.1	5.90×10^{1}	7.76×10^{1}	4.44×10^{1}
^{8}Li	80	2	17.7	19.1	16.4	3.10×10^{1}	4.95×10^{1}	1.87×10^{1}

†Angle and energy limits define the interval over which the cross section was averaged, whereas cross section limits are 68% confidence level limits on the cross section.

Species	Angle θ (deg)	±Δθ (deg)	Energy E (MeV/nucl)	E+ (MeV/nucl)	E- (MeV/nucl)	Cross Section σ (μb/MeV-sr)	σ+ (μb/MeV-sr)	σ- (μb/MeV-sr)
^{8}Li	80	2	24.7	25.9	23.6	3.60×10^{1}	7.10×10^{1}	1.60×10^{1}
^{8}Li	80	2	31.5	32.5	30.4	1.15×10^{1}	2.06×10^{1}	6.00×10^{0}
$^{(9)}Be^{*}$	55	5	30.0	31.6	28.9	1.99×10^{1}	2.31×10^{1}	1.67×10^{1}
$^{(9)}Be$	55	5	33.3	35.2	31.7	1.59×10^{1}	1.80×10^{1}	1.38×10^{1}
$^{(9)}Be$	55	5	37.2	38.5	36.0	6.80×10^{0}	9.50×10^{0}	4.80×10^{0}
$^{(9)}Be$	55	5	41.5	43.2	39.8	3.00×10^{0}	4.40×10^{0}	2.00×10^{0}
$^{(9)}Be$	65	5	30.2	31.6	28.9	7.30×10^{0}	9.80×10^{0}	5.40×10^{0}
$^{(9)}Be$	65	5	33.3	35.2	31.5	4.00×10^{0}	5.40×10^{0}	2.90×10^{0}
$^{(9)}Be$	65	5	37.2	38.5	36.0	6.20×10^{0}	8.80×10^{0}	4.30×10^{0}
$^{(9)}Be$	65	5	41.5	43.2	39.8	2.70×10^{0}	4.00×10^{0}	1.80×10^{0}
$^{(9)}Be$	75	5	27.5	29.5	25.4	7.20×10^{0}	8.50×10^{0}	5.90×10^{0}
$^{(9)}Be$	75	5	32.5	34.1	30.9	3.30×10^{0}	5.30×10^{0}	2.00×10^{0}
$^{(9)}Be$	75	5	38.0	39.8	36.2	3.10×10^{-1}	1.02×10^{0}	5.40×10^{-2}

*( ) denotes the isotope that was assumed in calculations where isotope resolution was not achieved.

Species	Angle θ (deg)	±Δθ (deg)	Energy E (MeV/nucl)	E+ (MeV/nucl)	E- (MeV/nucl)	Cross Section σ (μb/MeV-sr)	σ+ (μb/MeV-sr)	σ- (μb/MeV-sr)
$^{(9)}$Be	85	5	27.5	29.5	25.4	2.17×10^{0}	3.16×10^{0}	1.46×10^{0}
$^{(9)}$Be	85	5	32.5	34.1	30.9	3.90×10^{0}	6.00×10^{0}	2.46×10^{0}
$^{(9)}$Be	85	5	38.0	39.8	36.2	6.30×10^{-1}	1.46×10^{0}	2.20×10^{-1}
$^{(11)}$B	35	5	30.7	32.7	28.7	1.15×10^{1}	1.32×10^{1}	9.76×10^{0}
$^{(11)}$B	35	5	37.4	39.4	35.4	4.12×10^{0}	5.12×10^{0}	3.30×10^{0}
$^{(11)}$B	35	5	43.4	45.3	41.4	2.05×10^{0}	2.87×10^{0}	1.44×10^{0}
$^{(11)}$B	35	5	47.1	49.3	44.8	9.98×10^{-1}	1.38×10^{0}	7.15×10^{-1}
$^{(11)}$B	45	5	30.7	32.7	28.7	1.07×10^{1}	1.24×10^{1}	9.04×10^{0}
$^{(11)}$B	45	5	37.4	39.4	35.4	4.12×10^{0}	5.12×10^{0}	3.30×10^{0}
$^{(11)}$B	45	5	43.4	45.3	41.4	4.09×10^{0}	5.16×10^{0}	3.32×10^{0}
$^{(11)}$B	45	5	47.1	49.3	44.8	8.32×10^{-1}	1.19×10^{0}	5.74×10^{-1}
$^{(11)}$B	55	5	22.2	24.1	20.3	1.91×10^{1}	2.27×10^{1}	1.57×10^{1}
$^{(11)}$B	55	5	27.2	29.3	25.0	1.00×10^{1}	1.13×10^{1}	8.76×10^{0}
$^{(11)}$B	55	5	30.5	33.1	27.9	7.24×10^{0}	7.95×10^{0}	6.53×10^{0}
$^{(11)}$B	55	5	32.1	34.8	29.4	4.87×10^{0}	5.44×10^{0}	4.30×10^{0}

Species	Angle θ (deg)	±Δθ (deg)	Energy E (MeV/nucl)	E+ (MeV/nucl)	E- (MeV/nucl)	Cross Section σ (μb/MeV-sr)	σ+ (μb/MeV-sr)	σ- (μb/MeV-sr)
$^{(11)}B$	55	5	35.8	38.8	32.7	3.11×10^{0}	3.47×10^{0}	2.75×10^{0}
$^{(11)}B$	55	5	38.3	41.2	35.4	2.75×10^{0}	3.08×10^{0}	2.42×10^{0}
$^{(11)}B$	55	5	43.2	47.2	39.1	1.09×10^{0}	1.25×10^{0}	9.29×10^{-1}
$^{(11)}B$	55	5	47.4	50.0	44.8	1.09×10^{0}	1.41×10^{0}	8.37×10^{-1}
$^{(11)}B$	65	5	22.2	24.1	20.3	1.43×10^{1}	1.79×10^{1}	1.14×10^{1}
$^{(11)}B$	65	5	27.2	29.3	25.0	6.03×10^{0}	7.00×10^{0}	5.06×10^{0}
$^{(11)}B$	65	5	30.5	33.1	27.9	4.32×10^{0}	4.87×10^{0}	3.77×10^{0}
$^{(11)}B$	65	5	32.1	34.8	29.4	3.09×10^{0}	3.54×10^{0}	2.64×10^{0}
$^{(11)}B$	65	5	35.8	38.8	32.7	2.16×10^{0}	2.46×10^{0}	1.86×10^{0}
$^{(11)}B$	65	5	38.3	41.2	35.4	1.49×10^{0}	1.73×10^{0}	1.25×10^{0}
$^{(11)}B$	65	5	43.2	47.2	39.1	6.87×10^{-1}	8.15×10^{-1}	5.59×10^{-1}
$^{(11)}B$	65	5	47.4	50.0	44.8	3.63×10^{-1}	5.80×10^{-1}	2.19×10^{-1}
$^{(11)}B$	75	5	28.1	31.2	25.0	3.31×10^{0}	3.76×10^{0}	2.86×10^{0}
$^{(11)}B$	75	5	30.3	33.1	27.5	2.70×10^{0}	3.12×10^{0}	2.28×10^{0}
$^{(11)}B$	75	5	32.1	34.8	29.4	2.02×10^{0}	2.41×10^{0}	1.63×10^{0}

Species	Angle θ (deg)	±Δθ (deg)	Energy E (MeV/nucl)	E+ (MeV/nucl)	E- (MeV/nucl)	Cross Section σ (μb/MeV-sr)	σ+ (μb/MeV-sr)	σ- (μb/MeV-sr)
$^{(11)}B$	75	5	35.9	39.1	32.7	1.06×10^{0}	1.34×10^{0}	8.36×10^{-1}
$^{(11)}B$	75	5	38.5	41.2	35.7	5.09×10^{-1}	7.60×10^{-1}	3.33×10^{-1}
$^{(11)}B$	75	5	43.0	46.9	39.1	2.17×10^{-1}	3.34×10^{-1}	1.37×10^{-1}
$^{(11)}B$	85	5	28.1	31.2	25.0	1.96×10^{0}	2.31×10^{0}	1.61×10^{0}
$^{(11)}B$	85	5	30.3	33.1	27.5	1.32×10^{0}	1.69×10^{0}	1.03×10^{0}
$^{(11)}B$	85	5	32.1	34.8	29.4	7.47×10^{-1}	1.07×10^{0}	5.15×10^{-1}
$^{(11)}B$	85	5	35.9	39.1	32.7	3.85×10^{-1}	5.75×10^{-1}	2.52×10^{-1}
$^{(11)}B$	85	5	38.5	41.2	35.7	4.45×10^{-1}	6.85×10^{-1}	2.81×10^{-1}
$^{(11)}B$	85	5	43.0	46.9	39.1	1.55×10^{-1}	2.60×10^{-1}	8.96×10^{-2}
$^{(12)}C$	35	5	35.8	38.2	33.4	3.75×10^{0}	4.37×10^{0}	3.13×10^{0}
$^{(12)}C$	35	5	43.6	45.9	41.2	1.10×10^{0}	1.43×10^{0}	8.44×10^{-1}
$^{(12)}C$	35	5	50.6	52.8	48.3	7.65×10^{-1}	1.07×10^{0}	5.38×10^{-1}
$^{(12)}C$	35	5	54.9	57.5	52.2	2.72×10^{-1}	3.96×10^{-1}	1.83×10^{-1}
$^{(12)}C$	45	5	35.8	38.2	33.4	2.74×10^{0}	3.37×10^{0}	2.21×10^{0}
$^{(12)}C$	45	5	43.6	45.9	41.2	9.82×10^{-1}	1.29×10^{0}	7.38×10^{-1}

Species	Angle θ (deg)	±Δθ (deg)	Energy E (MeV/nucl)	E+ (MeV/nucl)	E- (MeV/nucl)	Cross Section σ (μb/MeV-sr)	σ+ (μb/MeV-sr)	σ- (μb/MeV-sr)
$^{(12)}C$	45	5	50.6	48.3	52.8	4.17×10^{-1}	6.66×10^{-1}	2.52×10^{-1}
$^{(12)}C$	45	5	54.9	57.5	52.2	2.12×10^{-1}	3.26×10^{-1}	1.34×10^{-1}
$^{(12)}C$	55	5	25.9	28.2	23.7	9.45×10^{0}	1.08×10^{1}	8.14×10^{0}
$^{(12)}C$	55	5	31.6	34.1	29.1	2.47×10^{0}	2.83×10^{0}	2.11×10^{0}
$^{(12)}C$	55	5	35.8	39.0	32.5	1.74×10^{0}	1.93×10^{0}	1.55×10^{0}
$^{(12)}C$	55	5	37.7	40.6	34.7	1.37×10^{0}	1.57×10^{0}	1.17×10^{0}
$^{(12)}C$	55	5	41.7	45.1	38.1	4.84×10^{-1}	5.70×10^{-1}	3.98×10^{-1}
$^{(12)}C$	55	5	44.7	48.1	41.2	4.76×10^{-1}	5.61×10^{-1}	3.91×10^{-1}
$^{(12)}C$	55	5	50.3	55.0	45.6	2.55×10^{-1}	3.02×10^{-1}	2.08×10^{-1}
$^{(12)}C$	55	5	55.3	58.4	52.2	1.20×10^{-1}	2.01×10^{-1}	6.82×10^{-2}
$^{(12)}C$	65	5	25.9	28.2	23.7	5.45×10^{0}	6.45×10^{0}	4.45×10^{0}
$^{(12)}C$	65	5	31.6	34.1	29.1	1.03×10^{0}	1.32×10^{0}	8.00×10^{-1}
$^{(12)}C$	65	5	35.8	39.0	32.5	6.37×10^{-1}	7.53×10^{-1}	5.21×10^{-1}
$^{(12)}C$	65	5	37.7	40.6	34.7	6.84×10^{-1}	8.54×10^{-1}	5.46×10^{-1}
$^{(12)}C$	65	5	41.7	45.2	38.1	2.27×10^{-1}	3.02×10^{-1}	1.69×10^{-1}

Species	Angle θ (deg)	±Δθ (deg)	Energy E (MeV/nucl)	E+ (MeV/nucl)	E- (MeV/nucl)	Cross Section σ (μb/MeV-sr)	σ+ (μb/MeV-sr)	σ- (μb/MeV-sr)
$^{(12)}C$	65	5	44.7	48.1	41.2	1.53×10^{-1}	2.18×10^{-1}	1.06×10^{-1}
$^{(12)}C$	65	5	50.3	55.0	45.6	8.49×10^{-2}	1.21×10^{-1}	5.86×10^{-2}
$^{(12)}C$	65	5	55.3	58.4	52.2	4.80×10^{-2}	1.11×10^{-1}	1.70×10^{-2}
$^{(12)}C$	75	5	32.8	36.4	29.1	7.23×10^{-1}	8.39×10^{-1}	6.07×10^{-1}
$^{(12)}C$	75	5	35.5	39.0	32.0	3.17×10^{-1}	4.14×10^{-1}	2.41×10^{-1}
$^{(12)}C$	75	5	37.7	40.6	34.7	3.04×10^{-1}	4.34×10^{-1}	2.10×10^{-1}
$^{(12)}C$	75	5	43.1	48.1	38.1	6.84×10^{-2}	1.02×10^{-1}	4.47×10^{-2}
$^{(12)}C$	75	5	50.2	54.7	45.6	9.65×10^{-3}	3.18×10^{-2}	1.67×10^{-3}
$^{(12)}C$	85	5	32.8	36.4	29.1	3.15×10^{-1}	4.11×10^{-1}	2.39×10^{-1}
$^{(12)}C$	85	5	35.5	39.0	32.0	2.45×10^{-1}	3.30×10^{-1}	1.76×10^{-1}
$^{(12)}C$	85	5	37.7	40.6	34.7	1.22×10^{-1}	2.18×10^{-1}	6.37×10^{-2}
$^{(12)}C$	85	5	43.1	48.1	38.1	8.55×10^{-3}	2.82×10^{-2}	1.48×10^{-3}
$^{(14)}N$	35	5	32.5	36.2	28.8	2.45×10^{0}	3.27×10^{0}	2.43×10^{0}
$^{(14)}N$	35	5	34.7	38.2	31.1	1.47×10^{0}	1.84×10^{0}	1.17×10^{0}
$^{(14)}N$	35	5	36.7	40.6	32.8	1.07×10^{0}	1.34×10^{0}	8.54×10^{-1}

Species	Angle θ (deg)	±Δθ (deg)	Energy E (MeV/nucl)	E+ (MeV/nucl)	E- (MeV/nucl)	Cross Section σ (μb/MeV-sr)	σ+ (μb/MeV-sr)	σ- (μb/MeV-sr)
$^{(14)}N$	35	5	40.5	45.1	35.8	4.98×10^{-1}	6.32×10^{-1}	3.90×10^{-1}
$^{(14)}N$	35	5	44.9	49.2	40.5	1.03×10^{-1}	1.84×10^{-1}	5.38×10^{-2}
$^{(14)}N$	45	5	32.5	36.2	28.8	1.40×10^{0}	1.76×10^{0}	1.11×10^{0}
$^{(14)}N$	45	5	34.7	38.2	31.1	1.40×10^{0}	1.77×10^{0}	1.10×10^{0}
$^{(14)}N$	45	5	36.7	40.6	32.8	6.69×10^{-1}	8.90×10^{-1}	4.98×10^{-1}
$^{(14)}N$	45	5	40.5	45.1	35.8	4.03×10^{-1}	5.26×10^{-1}	3.06×10^{-1}
$^{(14)}N$	45	5	44.9	49.2	40.5	7.73×10^{-2}	1.53×10^{-1}	3.52×10^{-2}
$^{(14)}N$	55	5	22.6	27.6	17.5	1.89×10^{0}	2.13×10^{0}	1.65×10^{0}
$^{(14)}N$	55	5	27.9	34.1	21.6	1.00×10^{0}	1.14×10^{0}	8.61×10^{-1}
$^{(14)}N$	55	5	33.0	37.2	28.8	1.19×10^{0}	1.41×10^{0}	9.69×10^{-1}
$^{(14)}N$	55	5	36.4	40.6	32.2	8.37×10^{-1}	1.06×10^{0}	6.60×10^{0}
$^{(14)}N$	55	5	40.5	45.1	35.8	2.13×10^{-1}	3.10×10^{-1}	1.43×10^{-1}
$^{(14)}N$	55	5	44.9	49.2	40.5	5.15×10^{-2}	1.19×10^{-1}	1.82×10^{-2}
$^{(14)}N$	65	5	22.6	27.6	17.5	1.57×10^{0}	1.79×10^{0}	1.35×10^{0}
$^{(14)}N$	65	5	27.9	34.1	21.6	4.64×10^{-1}	5.80×10^{-1}	3.70×10^{-1}

Species	Angle θ (deg)	±Δθ (deg)	Energy E (MeV/nucl)	E+ (MeV/nucl)	E- (MeV/nucl)	Cross Section σ (μb/MeV-sr)	σ+ (μb/MeV-sr)	σ- (μb/MeV-sr)
$^{(14)}N$	65	5	33.0	37.2	28.8	6.14×10^{-1}	8.17×10^{-1}	4.57×10^{-1}
$^{(14)}N$	65	5	36.4	40.6	32.2	3.42×10^{-1}	4.98×10^{-1}	2.30×10^{-1}
$^{(14)}N$	65	5	40.5	45.1	35.8	1.18×10^{-1}	1.98×10^{-1}	6.70×10^{-2}
$^{(14)}N$	80	10	22.6	27.6	17.5	2.65×10^{-1}	3.36×10^{-1}	2.08×10^{-1}
$^{(14)}N$	80	10	27.0	32.4	21.6	9.00×10^{-2}	1.39×10^{-1}	5.69×10^{-2}
$^{(14)}N$	80	10	31.6	36.2	27.0	3.39×10^{-2}	7.86×10^{-2}	1.20×10^{-2}
$^{(16)}O$	35	5	35.3	39.5	31.0	6.78×10^{-1}	7.83×10^{-1}	5.73×10^{-1}
$^{(16)}O$	35	5	37.9	41.7	34.1	4.51×10^{-1}	5.72×10^{-1}	3.54×10^{-1}
$^{(16)}O$	35	5	40.1	43.7	36.4	3.31×10^{-1}	4.45×10^{-1}	2.44×10^{-1}
$^{(16)}O$	35	5	43.5	48.5	38.5	2.52×10^{-1}	3.01×10^{-1}	2.03×10^{-1}
$^{(16)}O$	35	5	48.3	53.0	43.6	2.17×10^{-2}	5.03×10^{-2}	7.68×10^{-3}
$^{(16)}O$	45	5	35.3	39.5	31.0	4.68×10^{-1}	5.55×10^{-1}	3.81×10^{-1}
$^{(16)}O$	45	5	37.9	41.7	34.1	3.87×10^{-1}	5.02×10^{-1}	2.97×10^{-1}
$^{(16)}O$	45	5	40.1	43.7	36.4	1.42×10^{-1}	2.27×10^{-1}	8.58×10^{-2}
$^{(16)}O$	45	5	43.5	48.5	38.5	1.65×10^{-1}	2.15×10^{-1}	1.25×10^{-1}

Species	Angle θ (deg)	±Δθ (deg)	Energy E (MeV/nucl)	E+ (MeV/nucl)	E- (MeV/nucl)	Cross Section σ (μb/MeV-sr)	σ+ (μb/MeV-sr)	σ- (μb/MeV-sr)
$(16)_0$	45	5	48.3	53.0	43.6	3.26×10^{-2}	6.43×10^{-2}	1.49×10^{-2}
$(16)_0$	55	5	23.6	28.3	18.8	1.69×10^{0}	1.85×10^{0}	1.53×10^{0}
$(16)_0$	55	5	26.7	31.8	21.5	7.56×10^{-1}	8.58×10^{-1}	6.54×10^{-1}
$(16)_0$	55	5	30.8	36.1	25.5	4.94×10^{-1}	5.66×10^{-1}	4.22×10^{-1}
$(16)_0$	55	5	35.5	40.6	30.3	2.92×10^{-1}	3.48×10^{-1}	2.36×10^{-1}
$(16)_0$	55	5	39.5	43.7	35.2	2.33×10^{-1}	3.06×10^{-1}	1.75×10^{-1}
$(16)_0$	55	5	45.8	53.0	35.8	2.14×10^{-2}	3.83×10^{-2}	1.22×10^{-2}
$(16)_0$	65	5	23.6	28.3	18.8	1.12×10^{0}	1.25×10^{0}	9.86×10^{-1}
$(16)_0$	65	5	27.6	31.8	21.5	3.99×10^{-1}	4.73×10^{-1}	3.25×10^{-1}
$(16)_0$	65	5	30.8	36.1	25.5	2.52×10^{-1}	3.15×10^{-1}	2.01×10^{-1}
$(16)_0$	65	5	35.5	40.6	30.3	6.49×10^{-2}	1.04×10^{-1}	3.92×10^{-2}
$(16)_0$	65	5	39.5	43.7	35.2	4.36×10^{-2}	8.60×10^{-2}	1.99×10^{-2}
$(16)_0$	80	10	24.3	29.7	18.8	2.47×10^{-1}	2.83×10^{-1}	2.11×10^{-1}
$(16)_0$	80	10	28.2	33.1	23.2	1.21×10^{-1}	1.59×10^{-1}	9.10×10^{-2}
$(16)_0$	80	10	31.6	36.1	27.0	7.60×10^{-2}	1.13×10^{-1}	4.97×10^{-2}

Species	Angle θ (deg)	±Δθ (deg)	Energy E (MeV/nucl)	E+ (MeV/nucl)	E- (MeV/nucl)	Cross Section σ (μb/MeV-sr)	σ+ (μb/MeV-sr)	σ- (μb/MeV-sr)
$(16)_O$	80	10	34.4	39.0	29.7	4.72×10^{-2}	7.91×10^{-2}	2.68×10^{-2}
$(19)_F$	40	10	22.8	27.3	18.3	5.40×10^{-1}	6.40×10^{-1}	4.40×10^{-1}
$(19)_F$	40	10	26.3	30.3	22.2	3.20×10^{-1}	4.20×10^{-1}	2.40×10^{-1}
$(19)_F$	40	10	31.1	35.1	27.1	1.80×10^{-1}	2.60×10^{-1}	1.20×10^{-1}
$(19)_F$	40	10	36.5	40.9	32.1	8.42×10^{-2}	1.05×10^{-1}	6.75×10^{-2}
$(19)_F$	40	10	39.5	43.7	35.2	6.46×10^{-2}	8.30×10^{-2}	4.95×10^{-2}
$(19)_F$	40	10	41.8	45.3	38.2	4.38×10^{-2}	6.74×10^{-2}	2.77×10^{-2}
$(19)_F$	40	10	47.4	54.9	39.9	9.40×10^{-3}	1.37×10^{-2}	6.33×10^{-3}
$(19)_F$	55	5	17.3	22.5	12.2	2.76×10^{0}	3.63×10^{0}	2.08×10^{0}
$(19)_F$	55	5	24.4	29.3	19.4	2.88×10^{-1}	3.30×10^{-1}	2.46×10^{-1}
$(19)_F$	55	5	27.6	32.9	22.2	1.38×10^{-1}	1.65×10^{-1}	1.11×10^{-1}
$(19)_F$	55	5	31.9	37.4	26.3	6.02×10^{-2}	8.10×10^{-2}	4.43×10^{-2}
$(19)_F$	55	5	38.4	45.3	31.4	2.18×10^{-2}	3.25×10^{-2}	1.43×10^{-2}
$(19)_F$	55	5	47.4	54.9	39.9	4.17×10^{-3}	9.67×10^{-3}	1.48×10^{-3}
$(19)_F$	65	5	17.3	22.5	12.2	8.60×10^{-1}	1.44×10^{0}	4.90×10^{-1}

Species	Angle θ (deg)	±Δθ (deg)	Energy E (MeV/nucl)	E+ (MeV/nucl)	E- (MeV/nucl)	Cross Section σ (μb/MeV-sr)	σ+ (μb/MeV-sr)	σ- (μb/MeV-sr)
$^{(19)}F$	65	5	24.4	29.3	19.4	1.74×10^{-1}	2.06×10^{-1}	1.42×10^{-1}
$^{(19)}F$	65	5	27.6	32.9	22.2	4.25×10^{-2}	6.35×10^{-2}	2.78×10^{-2}
$^{(19)}F$	65	5	31.9	37.4	26.3	4.30×10^{-2}	6.14×10^{-2}	2.97×10^{-2}
$^{(19)}F$	65	5	38.4	45.3	31.4	8.16×10^{-3}	1.61×10^{-2}	3.72×10^{-3}
$^{(19)}F$	80	10	19.4	25.2	13.6	1.40×10^{-1}	2.30×10^{-1}	7.90×10^{-2}
$^{(19)}F$	80	10	24.7	30.0	19.4	4.23×10^{-2}	5.37×10^{-2}	3.32×10^{-2}
$^{(19)}F$	80	10	28.7	34.2	23.1	1.60×10^{-2}	2.46×10^{-2}	1.01×10^{-2}
$^{(19)}F$	80	10	34.2	40.4	27.9	1.59×10^{-3}	5.25×10^{-3}	2.75×10^{-4}
$^{(20)}Ne$	35	5	24.0	28.0	20.0	8.60×10^{-1}	1.03×10^{0}	6.90×10^{-1}
$^{(20)}Ne$	35	5	28.3	32.3	24.2	2.70×10^{-1}	3.60×10^{-1}	2.00×10^{-1}
$^{(20)}Ne$	35	5	31.7	35.4	27.9	2.10×10^{-1}	3.00×10^{-1}	1.45×10^{-1}
$^{(20)}Ne$	35	5	34.4	38.3	30.4	5.10×10^{-2}	1.00×10^{-1}	2.30×10^{-2}
$^{(20)}Ne$	45	5	24.0	28.0	20.0	5.70×10^{-1}	7.40×10^{-1}	4.30×10^{-1}
$^{(20)}Ne$	45	5	28.3	32.3	24.2	2.90×10^{-1}	3.90×10^{-1}	2.20×10^{-1}
$^{(20)}Ne$	45	5	31.7	35.4	27.9	1.70×10^{-1}	2.50×10^{-1}	1.10×10^{-1}

Species	Angle θ (deg)	±Δθ (deg)	Energy E (MeV/nucl)	E+ (MeV/nucl)	E- (MeV/nucl)	Cross Section σ (μb/MeV-sr)	σ+ (μb/MeV-sr)	σ- (μb/MeV-sr)
$^{(20)}$Ne	45	5	34.4	38.3	30.4	6.80×10^{-2}	1.22×10^{-1}	3.50×10^{-2}
$^{(20)}$Ne	55	5	19.0	24.6	13.3	2.12×10^{0}	2.49×10^{0}	1.74×10^{0}
$^{(20)}$Ne	55	5	24.3	28.5	20.0	4.80×10^{-1}	6.20×10^{-1}	3.70×10^{-1}
$^{(20)}$Ne	55	5	28.5	32.7	24.2	2.70×10^{-1}	3.60×10^{-1}	2.00×10^{-1}
$^{(20)}$Ne	55	5	31.9	35.8	27.9	4.30×10^{-2}	1.00×10^{-1}	1.50×10^{-2}
$^{(20)}$Ne	55	5	34.6	38.7	30.4	0.00×10^{0}	3.00×10^{-2}	0.00×10^{0}
$^{(20)}$Ne	65	5	19.0	24.6	13.3	1.19×10^{0}	1.54×10^{0}	9.10×10^{-1}
$^{(20)}$Ne	65	5	24.3	28.5	20.0	3.30×10^{-1}	4.50×10^{-1}	2.40×10^{-1}
$^{(20)}$Ne	65	5	28.5	32.7	24.2	1.16×10^{-1}	1.85×10^{-1}	7.00×10^{-2}
$^{(20)}$Ne	65	5	31.9	38.3	30.4	4.30×10^{-2}	9.90×10^{-2}	1.50×10^{-2}
$^{(20)}$Ne	65	5	34.6	28.0	20.0	0.00×10^{0}	3.00×10^{-2}	0.00×10^{0}
$^{(20)}$Ne	75	5	20.7	32.3	24.2	6.20×10^{-1}	7.40×10^{-1}	5.10×10^{-1}
$^{(20)}$Ne	75	5	24.1	35.4	27.9	2.50×10^{-1}	3.60×10^{-1}	1.70×10^{-1}
$^{(20)}$Ne	75	5	27.0	38.3	30.4	6.90×10^{-2}	1.16×10^{-1}	3.80×10^{-2}
$^{(20)}$Ne	85	5	20.7	24.6	13.3	2.60×10^{-1}	3.60×10^{-1}	1.90×10^{-1}

Species	Angle θ (deg)	±Δθ (deg)	Energy E (MeV/nucl)	E+ (MeV/nucl)	E- (MeV/nucl)	Cross Section σ (μb/MeV-sr)	σ+ (μb/MeV-sr)	σ- (μb/MeV-sr)
$^{(20)}Ne$	85	5	24.1	28.5	20.0	7.40×10^{-2}	1.46×10^{-1}	3.40×10^{-2}
$^{(20)}Ne$	85	5	27.0	32.7	24.2	0.00×10^{0}	2.50×10^{-2}	0.00×10^{0}
$^{(23)}Na$	40	10	24.6	35.8	27.9	1.31×10^{-1}	1.64×10^{-1}	1.04×10^{-1}
$^{(23)}Na$	40	10	29.0	38.7	30.4	4.30×10^{-2}	5.90×10^{-2}	3.10×10^{-2}
$^{(23)}Na$	40	10	32.5	24.6	13.3	1.80×10^{-2}	3.00×10^{-2}	1.00×10^{-2}
$^{(23)}Na$	40	10	35.3	28.5	20.0	1.20×10^{-2}	2.10×10^{-2}	6.30×10^{-3}
$^{(23)}Na$	60	10	19.4	32.7	24.2	3.15×10^{-1}	3.75×10^{-1}	2.55×10^{-1}
$^{(23)}Na$	60	10	24.9	29.2	20.5	4.30×10^{-2}	6.10×10^{-2}	3.00×10^{-2}
$^{(23)}Na$	60	10	29.2	33.6	24.8	4.30×10^{-2}	5.90×10^{-2}	3.10×10^{-2}
$^{(23)}Na$	60	10	34.2	39.7	28.6	3.20×10^{-3}	7.40×10^{-3}	1.10×10^{-3}
$^{(23)}Na$	80	10	21.3	27.3	15.2	7.30×10^{-2}	9.30×10^{-2}	5.70×10^{-2}
$^{(23)}Na$	80	10	25.8	31.1	20.5	2.60×10^{-2}	4.20×10^{-2}	1.60×10^{-2}
$^{(23)}Na$	80	10	28.2	33.7	22.7	3.20×10^{-3}	1.10×10^{-2}	5.50×10^{-4}

Figure Captions

Figure 1. Drawing of two etched particle tracks for the last three Lexan sheets at the end of range of the particle. The left particle would be detected in this experiment by the hole in the middle sheet. The right particle would not be detected.

Figure 2. Plot of the detection efficiency vs. etch time for charges $4 \leq Z \leq 9$ using standard UV exposure.

Figure 3. Plot of etch rate V_T vs. average range $\bar{R}$ for 500 events from the 30 hr etch.

Figure 4. Histograms for number of events vs. etch rate for the four different UV and etch times used in this experiment. There is approximate vertical alignment of the first three sets of histograms. The fourth set is shifted because of the shorter UV exposure.

Figure 5. Plot of data for charges $3 \leq Z \leq 11$ differential cross section vs. energy/nucleon. Data at some intermediate angles are omitted to avoid clutter.

a) ^{8}Li, Be, B

b) C, N, O

c) F, Ne, Na

Figure 6. Plot of the energy spectrum of all species at a lab angle of 55°.

Figure 7. Plot of the angular distribution of Boron for three different energy intervals.

Figure 8. Plot of the 400 MeV/nucl ^{20}Ne + U data of ref. 8, differential cross section vs. energy/nucleon.

Figure 9. 90% confidence interval boundaries on values of the two parameters to a thermal fit to the data, the source velocity β_o and the temperature τ_o.

Figure 10. Plot of all possible combinations of β_o and τ_o assuming no transparency $\varepsilon = 0$ and 50% transparency $\varepsilon = 0.5$. The box at low β_o contains all the 90% confidence intervals of Fig. 8.

Figure 11. Same figure as Fig. 9 except the theoretical curves of Fig. 10 are shown.

Figure 12. Plot of proton cross sections from 500 MeV/nucl ^{40}Ar + Au → P + X assuming the final state interaction model and using the ^{40}Ar + Au → Ne + X data. Proton data from ref. 9, 250 and 400 MeV/nucl ^{20}Ne + U → P + X are shown for comparison.

Figure 13. Boron cross section from 500 MeV/nucl ^{40}Ar + Au → B + X assuming the final state interaction model and using the calculated proton spectrum of Fig. 12. The measured B data are shown for comparison.

Figure 14. Calculated oxygen spectrum for 500 MeV/nucl ^{40}Ar + Au → O + X assuming the spinning target explosion model developed in this paper.

Figure 15. Calculated oxygen spectrum assuming the expanding target explosion model developed in this paper. Taking parameter values $\alpha = 0.5$, $t_d = t_b$, that is no early decoupling from the nucleon gas.

Figure 16. Calculated oxygen spectrum assuming the expanding target explosion model developed in this paper. Taking parameter values $\alpha = 10.0$, $t_d = 5t_b$, that is early decoupling and $\epsilon = 0.3$.

Figure 17. a) Plot of elasticity vs. impact parameter and target recoil β vs. impact parameter for 500 MeV/nucl ^{40}Ar + Au.

b) Plot of target internal energy/nucleon vs. impact parameter and target angular momentum vs. impact parameter for 500 MeV/nucl ^{40}Ar + Au.

Figure 18. Oxygen fragment spectrum calculated for four different models. Results were averaged over all impact parameters using the results of Fig. 17.

Figure 19. Same as Fig. 18 except the impact parameter average excluded the most central 20% of the cross section.

Figure 20. Plot of the invariant cross section vs. momentum P' in a source frame recoiling with velocity $\beta = 0.08$. The points are for all species, angles and energies. For the 500 MeV/nucl ^{40}Ar + Au and 400 MeV/nucl ^{20}Ne + U data of refs. 8 and 16.

Figure 21. Plots of contours of constant invariant cross section in transverse momentum $P_\perp$ vs. longitudinal momentum $P_\parallel$ space.

a) ^{6}Li, Be, B

b) C, N, O

c) F, Ne, Na

Circles drawn through the data are "eyeball" fits.

Figure 22. Plots of invariant cross sections vs. radii of the momentum circles P' of Fig. 21 also data from similar calculations for 400 MeV/nucl ^{20}Ne + U and 2100 MeV/nucl C + Au of refs. 7, 8, 16, and 25.

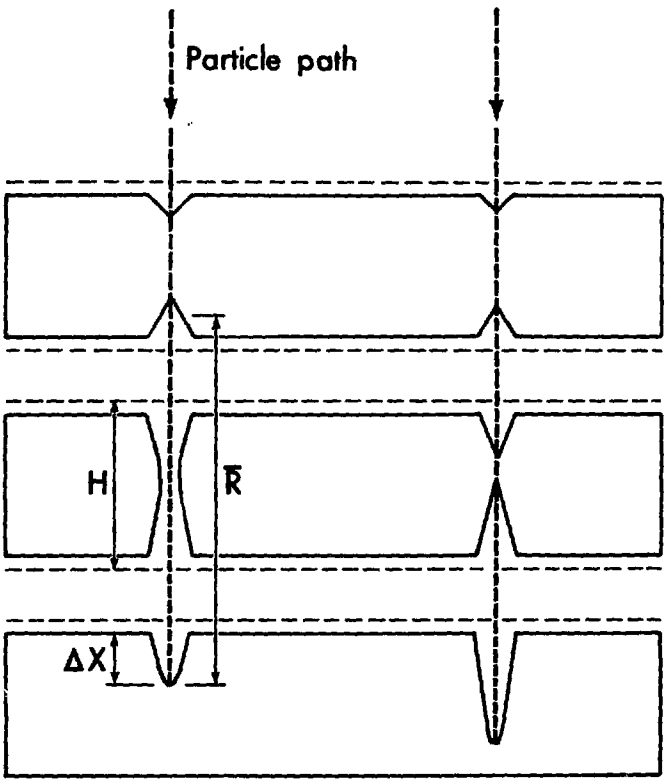

Fig. 1

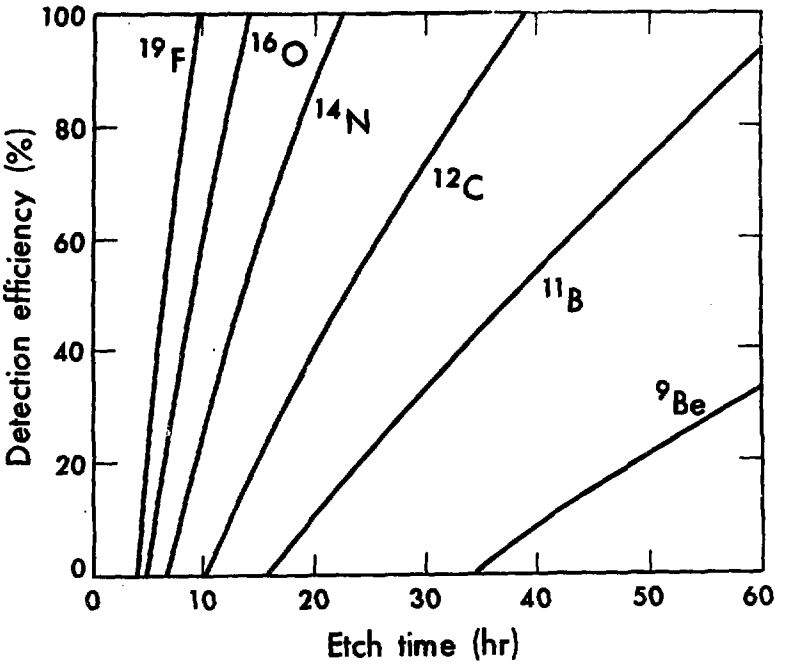
100
80
60
40
20
0
Detection efficiency (%)
0
10
20
30
40
50
60
Etch time (hr)
19F
16O
14N
12C
11B
9Be

Fig. 2

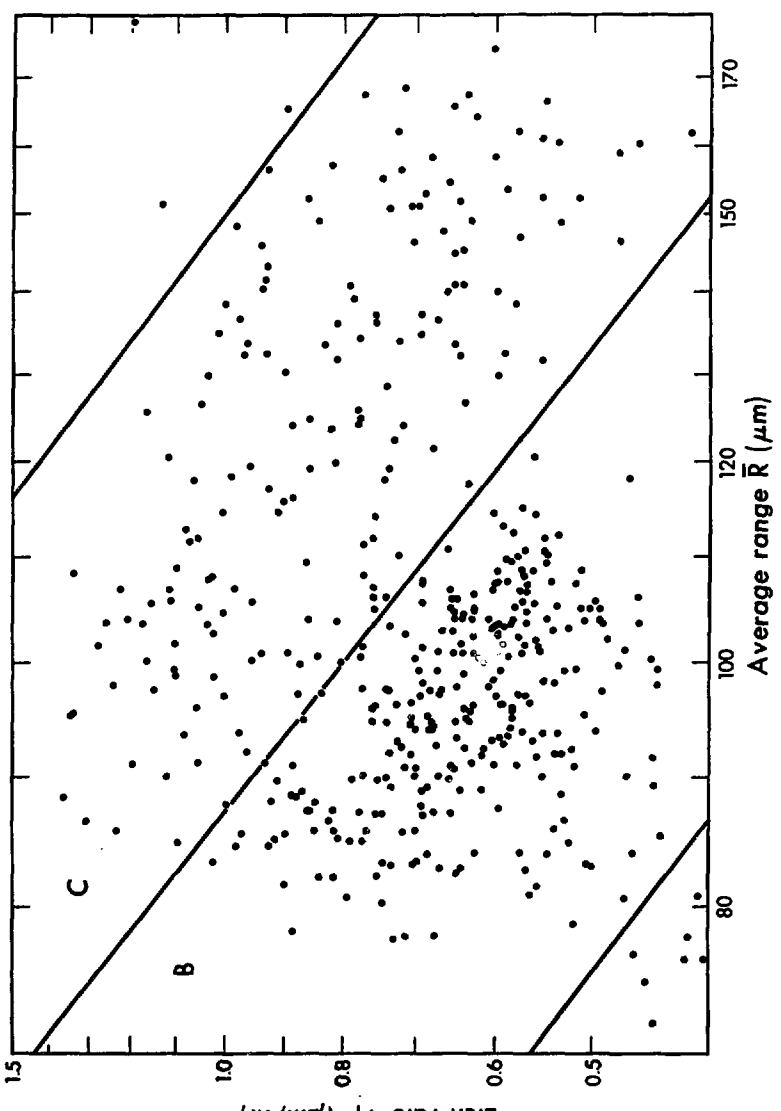
Etch rate V_t^* (μm/hr)
1.5
1.0
0.8
0.6
0.5
C
B
80
100
120
150
170
Average range $\bar{R}$ (μm)

Fig. 3

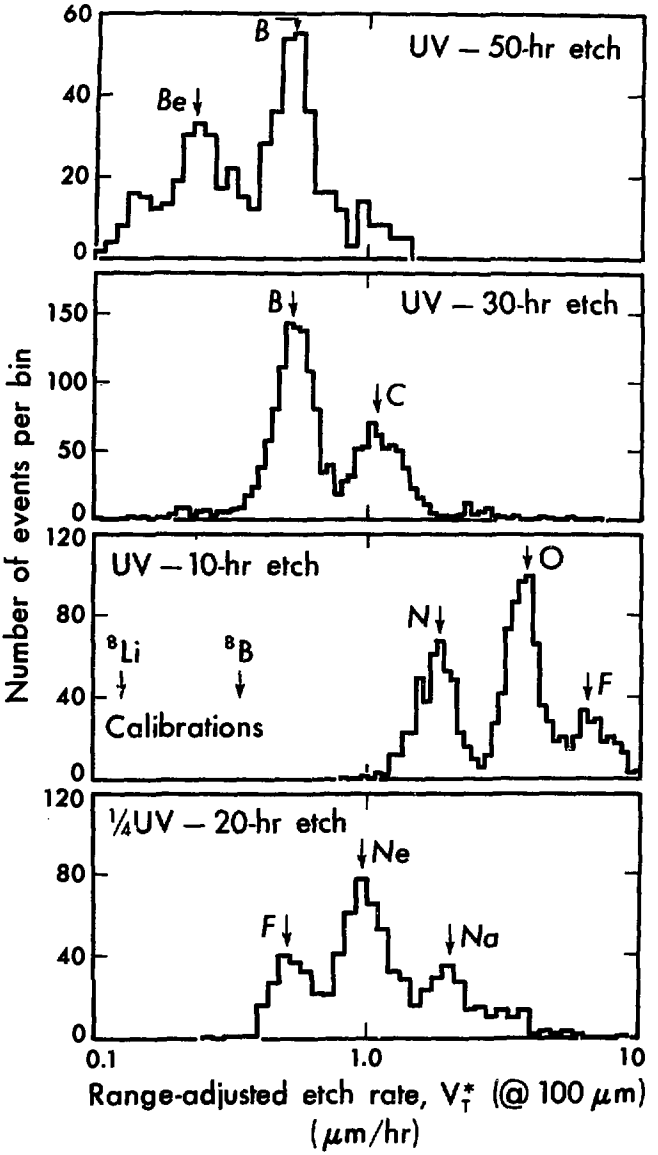
UV – 50-hr etch
B
Be
UV – 30-hr etch
B
C
UV – 10-hr etch
O
N
F
⁸Li
⁸B
Calibrations
¼UV – 20-hr etch
Ne
F
Na
Number of events per bin
Range-adjusted etch rate, V_T* (@ 100 μm)
(μm/hr)

Fig. 4

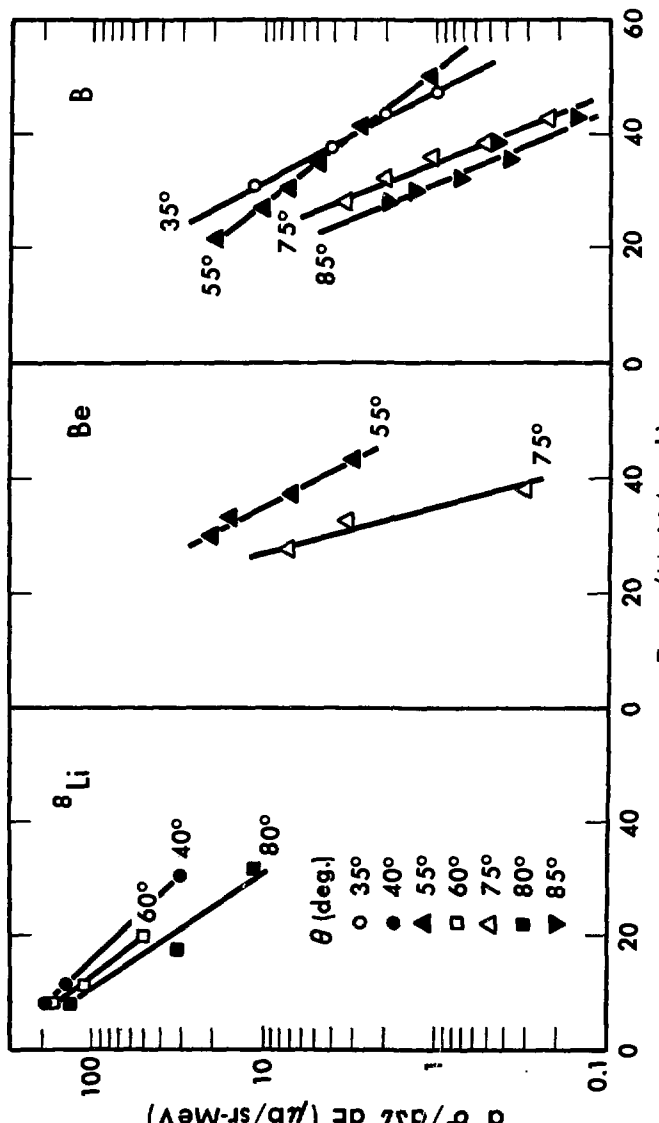
$d^2\sigma/d\Omega\ dE$ (μb/sr-MeV)
100
10
1
0.1
^{8}Li
Be
B
θ (deg.)
35°
40°
55°
60°
75°
80°
85°
E_{LAB} (MeV/nucl.)
0
20
40
60

Fig. 5(a)

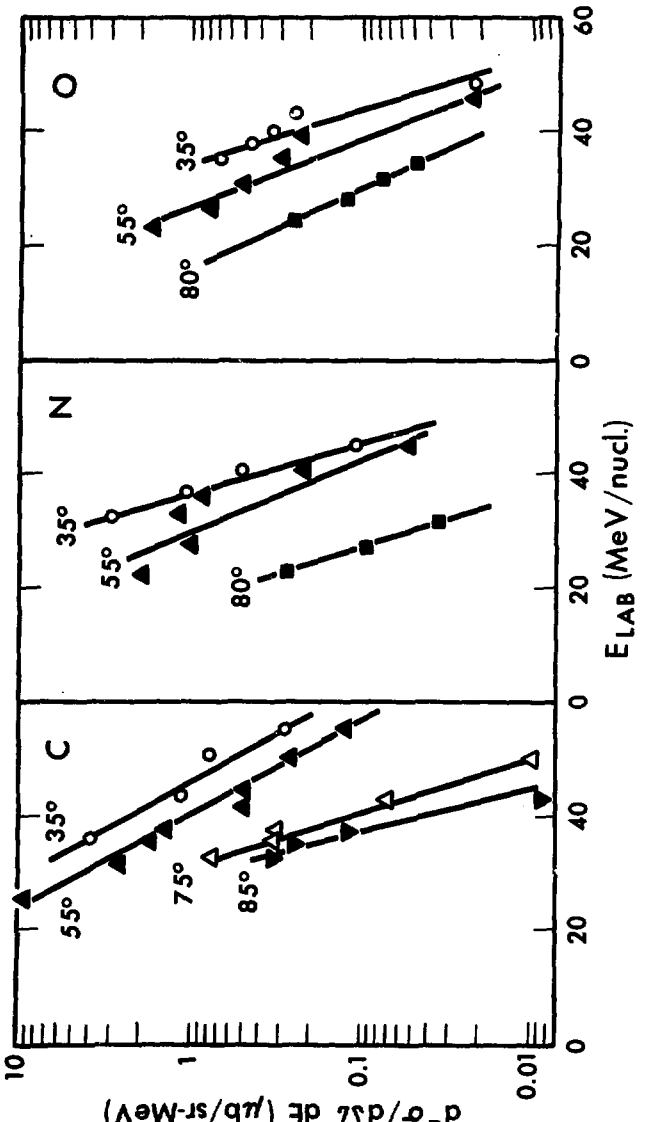
C
N
O
35°
55°
75°
85°
80°
10
1
0.1
0.01
0
20
40
60
$d^2\sigma/d\Omega\, dE$ (μb/sr-MeV)
E_{LAB} (MeV/nucl.)

Fig. 5(b)

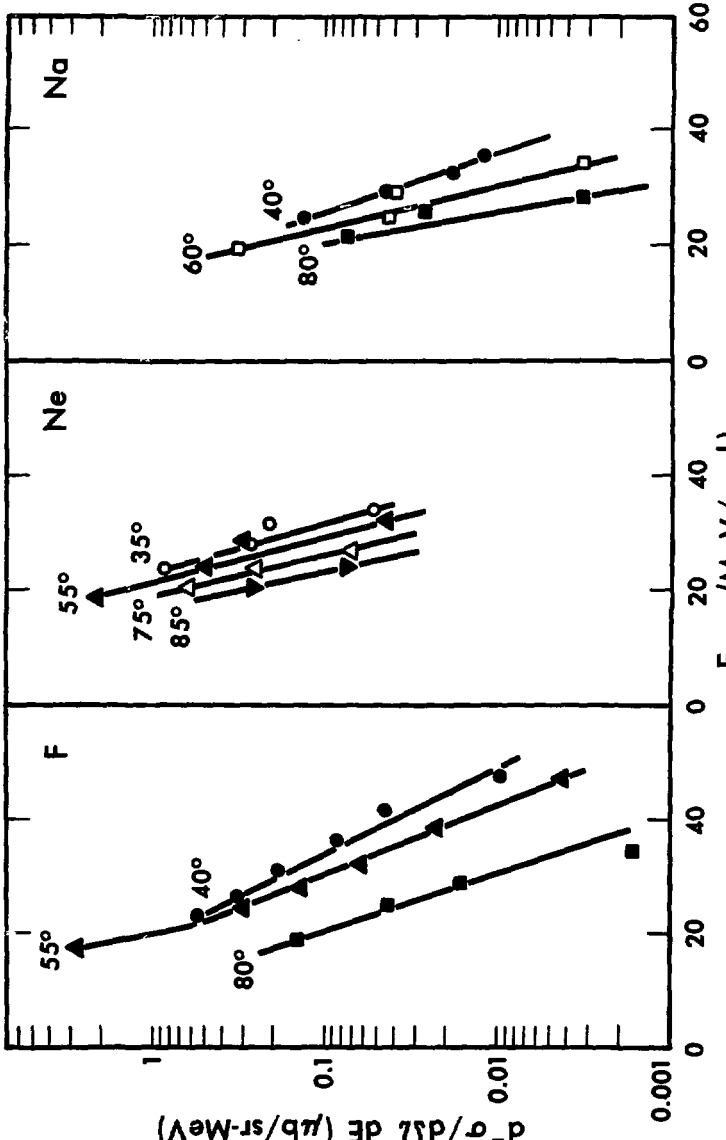
F
Ne
Na
55°
40°
80°
35°
75°
85°
60°
0
20
40
60
1
0.1
0.01
0.001
$d^2\sigma/d\Omega\, dE$ (μb/sr-MeV)
E_{LAB} (MeV/nucl.)

Fig. 5(c)

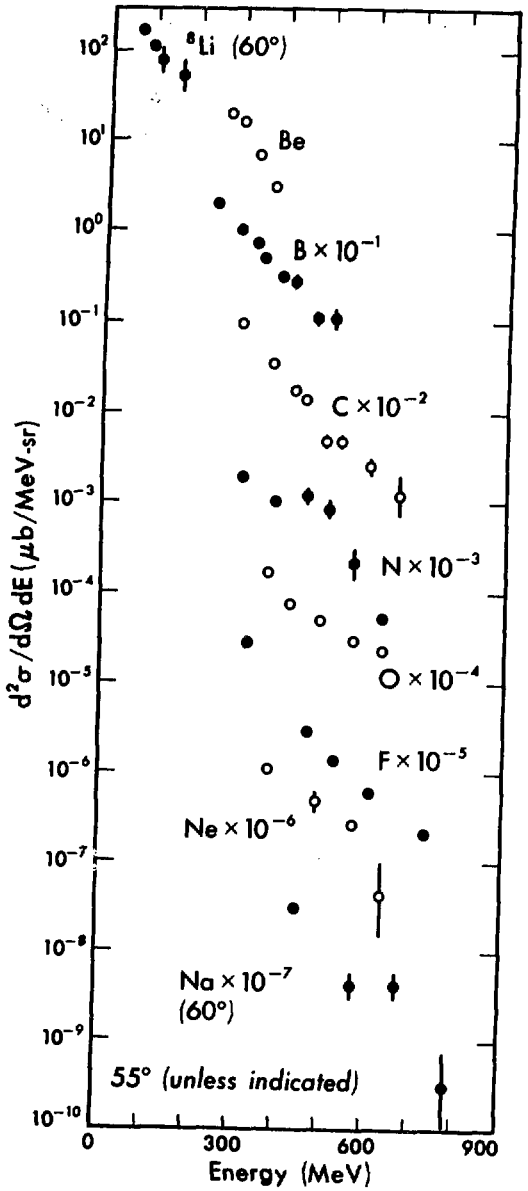
^{8}Li (60°)
Be
B × 10^{-1}
C × 10^{-2}
N × 10^{-3}
O × 10^{-4}
F × 10^{-5}
Ne × 10^{-6}
Na × 10^{-7}
(60°)
55° (unless indicated)
d$^2\sigma$/dΩ dE (μb/MeV-sr)
Energy (MeV)
10^2
10^1
10^0
10^{-1}
10^{-2}
10^{-3}
10^{-4}
10^{-5}
10^{-6}
10^{-7}
10^{-8}
10^{-9}
10^{-10}
0
300
600
900

Fig. 6

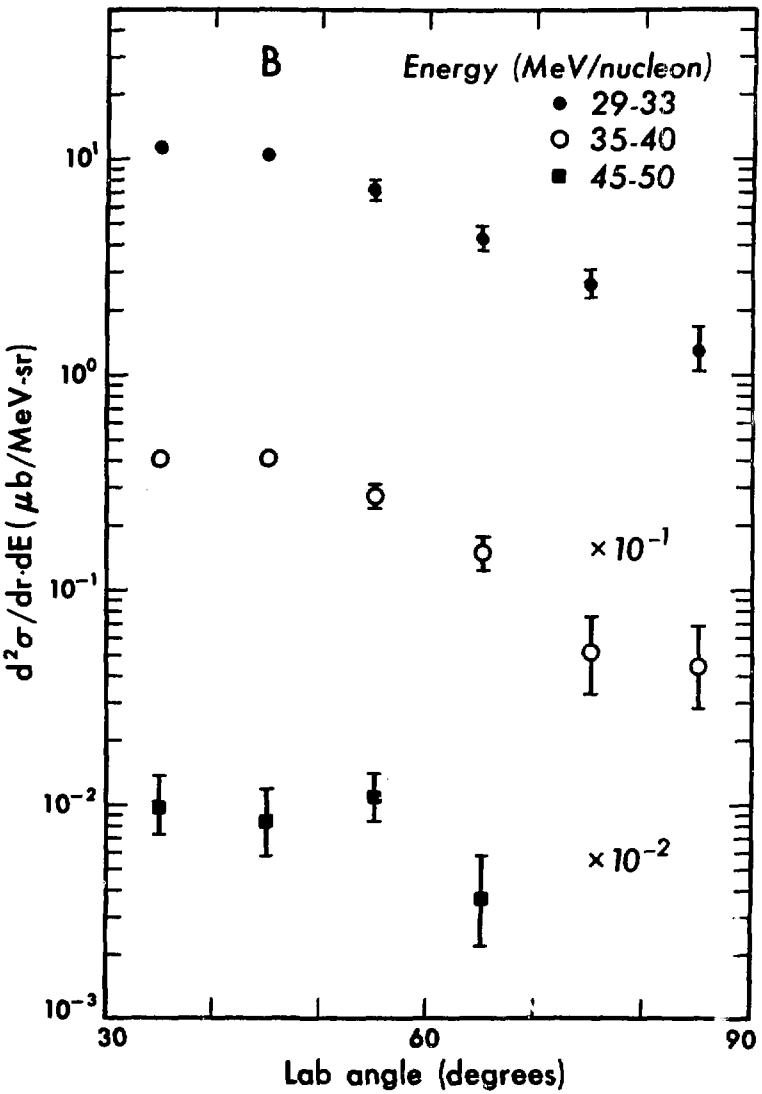
B
Energy (MeV/nucleon)
29-33
35-40
45-50
$\times 10^{-1}$
$\times 10^{-2}$
$d^2\sigma/dr\cdot dE$ (μb/MeV-sr)
10^1
10^0
10^{-1}
10^{-2}
10^{-3}
30
60
90
Lab angle (degrees)

Fig. 7

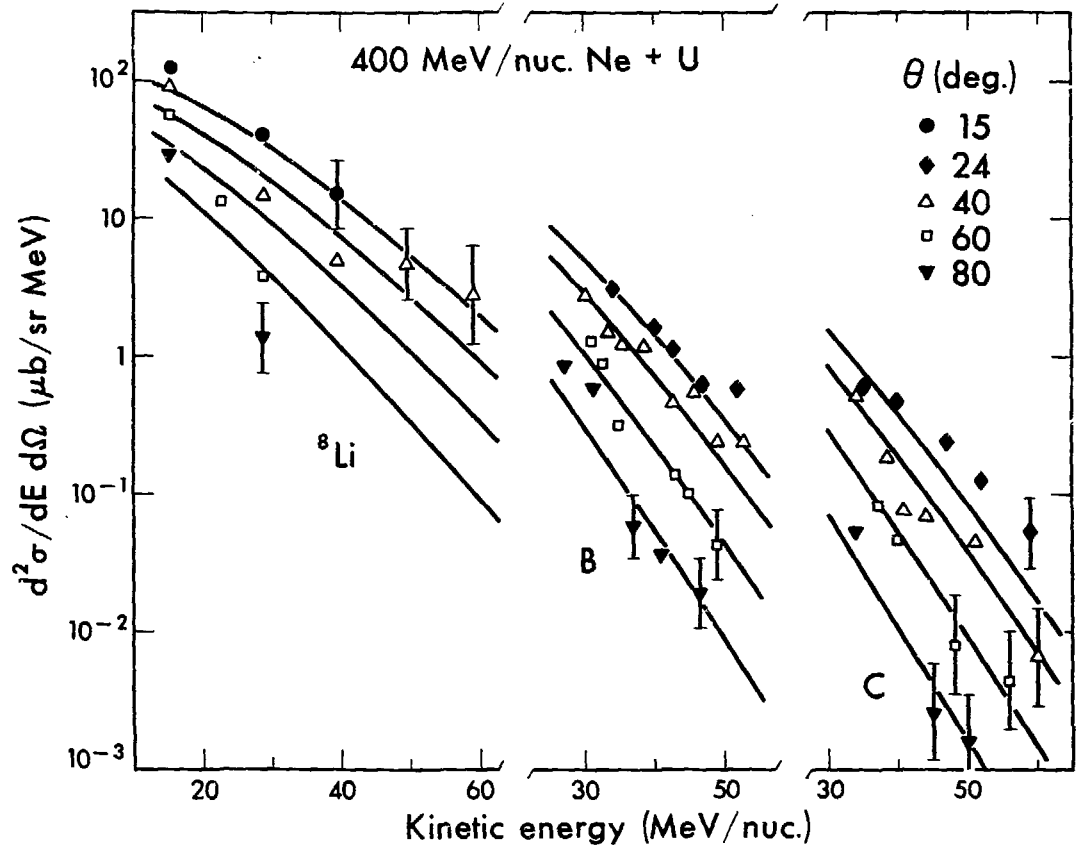
400 MeV/nuc. Ne + U
θ (deg.)
15
24
40
60
80
$d^2\sigma/dE\,d\Omega$ (μb/sr MeV)
10^2
10
1
10^{-1}
10^{-2}
10^{-3}
^{8}Li
B
C
20
40
60
30
50
30
50
Kinetic energy (MeV/nuc.)

Fig. 8

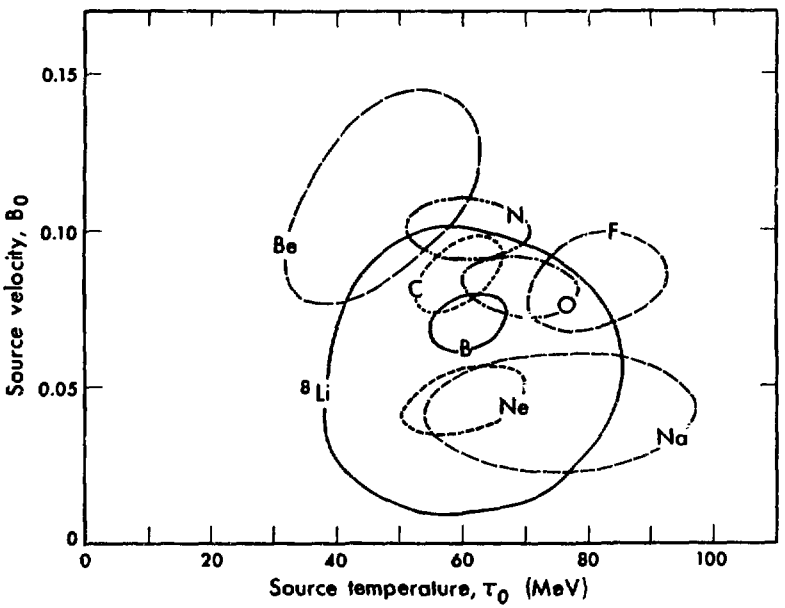
0.15
0.10
0.05
0
Source velocity, B_0
0
20
40
60
80
100
Source temperature, T_0 (MeV)
Be
N
F
C
O
B
^{8}Li
Ne
Na

Fig. 9

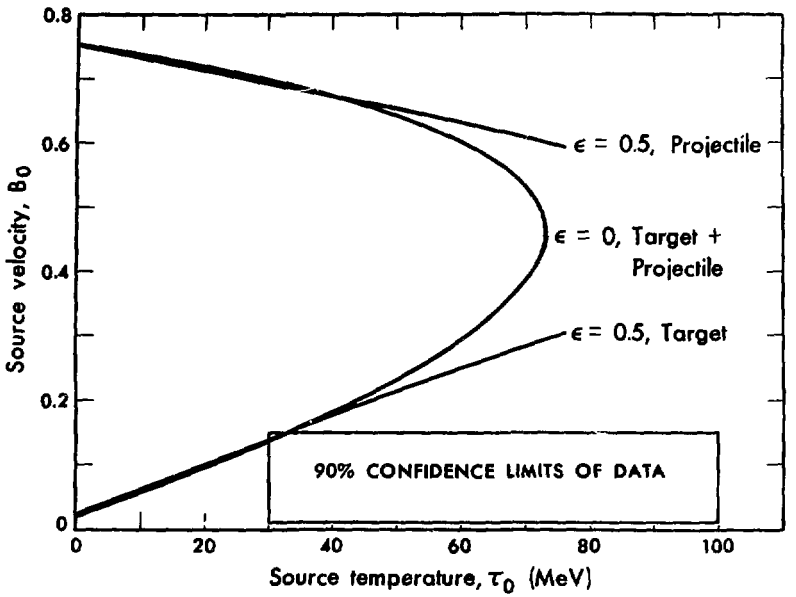
0.8
0.6
0.4
0.2
0
Source velocity, β_0
0
20
40
60
80
100
Source temperature, τ_0 (MeV)
ϵ = 0.5, Projectile
ϵ = 0, Target + Projectile
ϵ = 0.5, Target
90% CONFIDENCE LIMITS OF DATA

Fig. 10

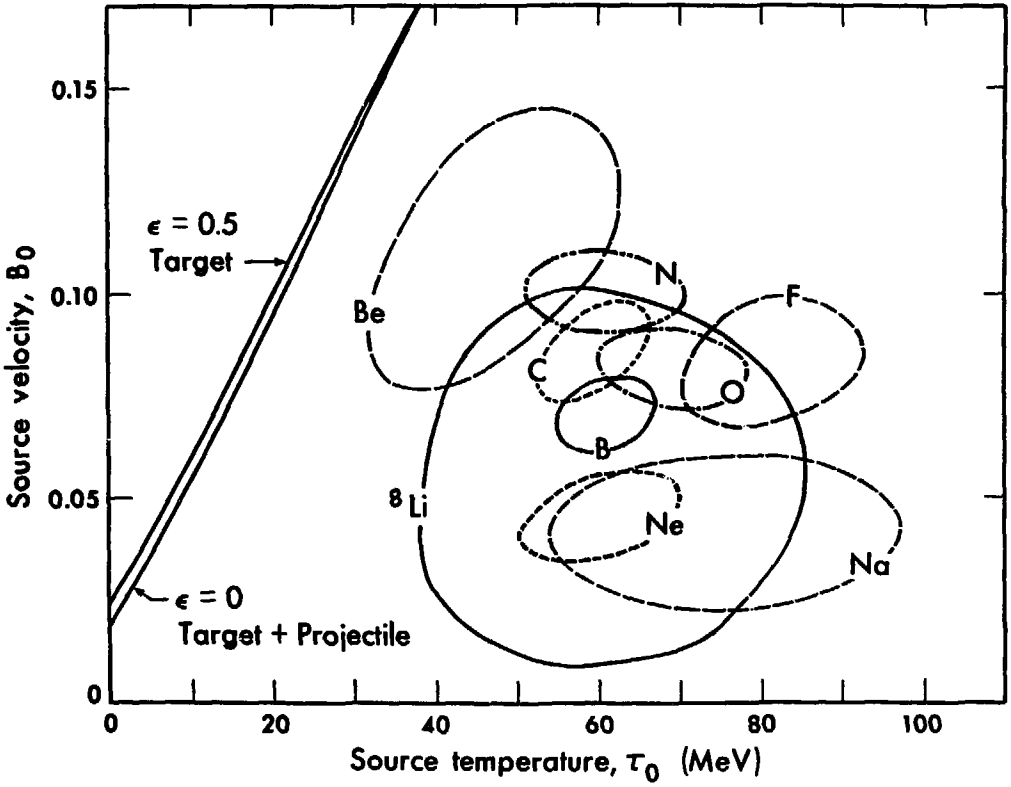
0.15
0.10
0.05
0
Source velocity, B_0
$\epsilon = 0.5$
Target
$\epsilon = 0$
Target + Projectile
Be
N
F
C
O
B
^{8}Li
Ne
Na
0
20
40
60
80
100
Source temperature, τ_0 (MeV)

Fig. 11

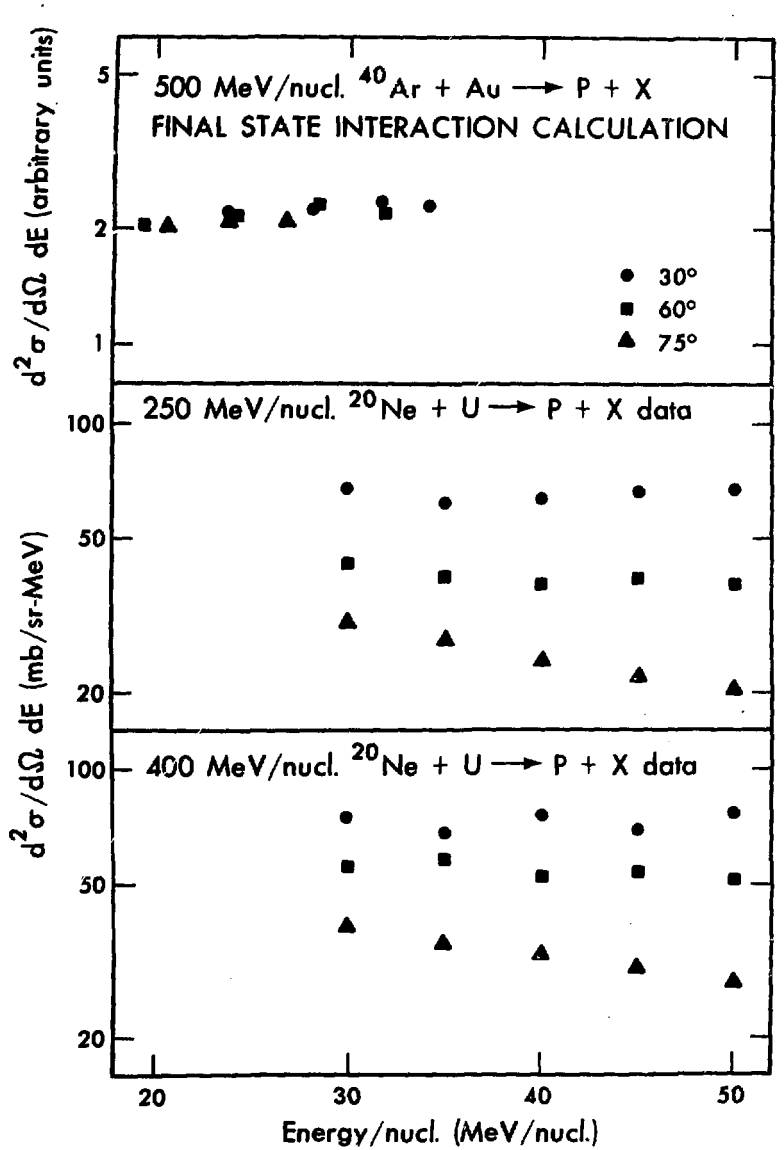
500 MeV/nucl. ^{40}Ar + Au → P + X
FINAL STATE INTERACTION CALCULATION
30°
60°
75°
250 MeV/nucl. ^{20}Ne + U → P + X data
400 MeV/nucl. ^{20}Ne + U → P + X data
$d^2\sigma/d\Omega\, dE$ (arbitrary units)
$d^2\sigma/d\Omega\, dE$ (mb/sr-MeV)
Energy/nucl. (MeV/nucl.)

Fig. 12

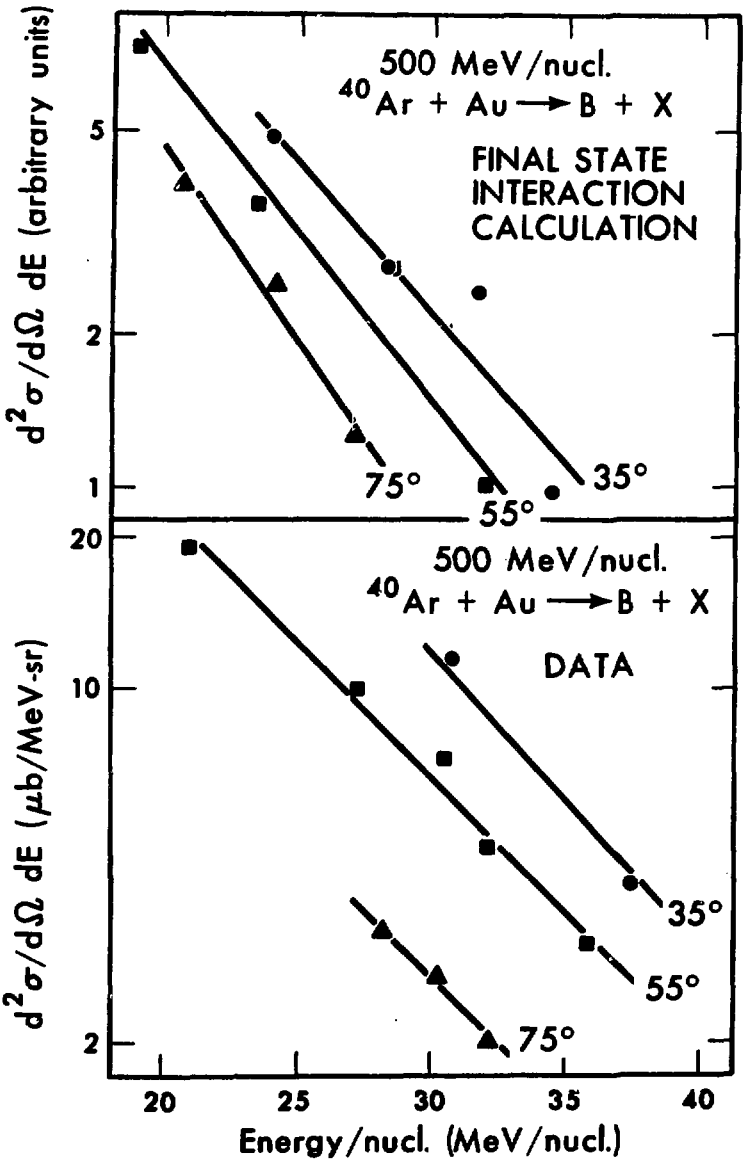
500 MeV/nucl.
40Ar + Au → B + X
FINAL STATE
INTERACTION
CALCULATION
35°
55°
75°
d2σ/dΩ dE (arbitrary units)
500 MeV/nucl.
40Ar + Au → B + X
DATA
35°
55°
75°
d2σ/dΩ dE (μb/MeV-sr)
Energy/nucl. (MeV/nucl.)

Fig. 13

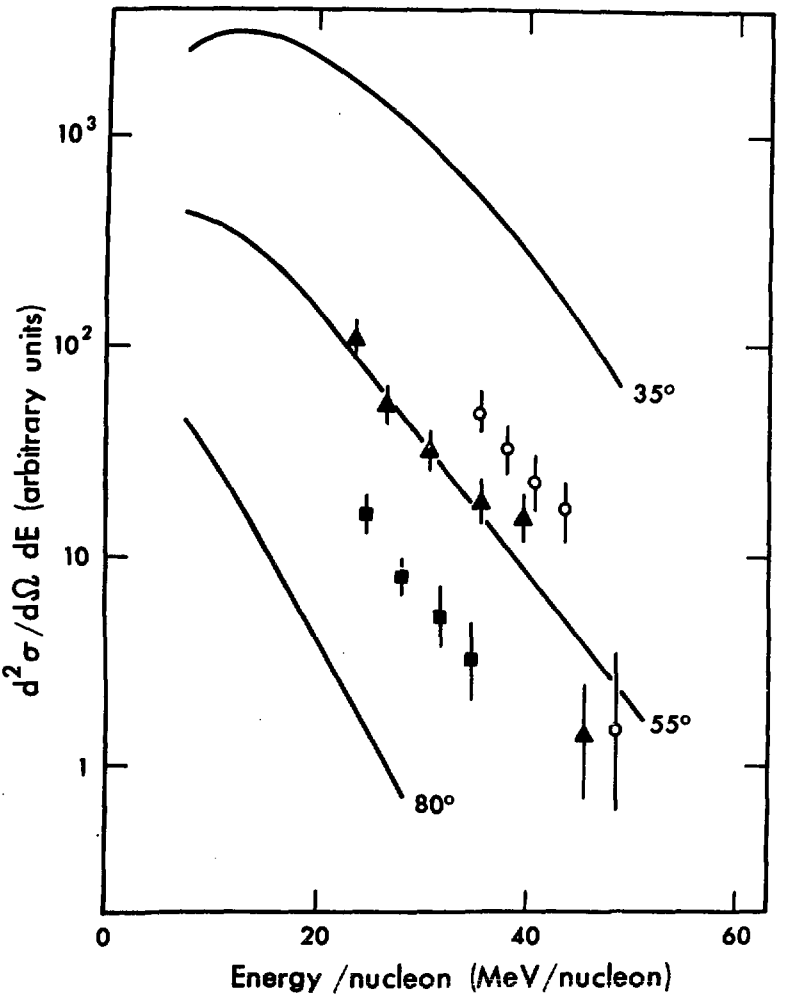
10^3
10^2
10
1
$d^2\sigma/d\Omega\, dE$ (arbitrary units)
35°
55°
80°
0
20
40
60
Energy /nucleon (MeV/nucleon)

Fig. 14

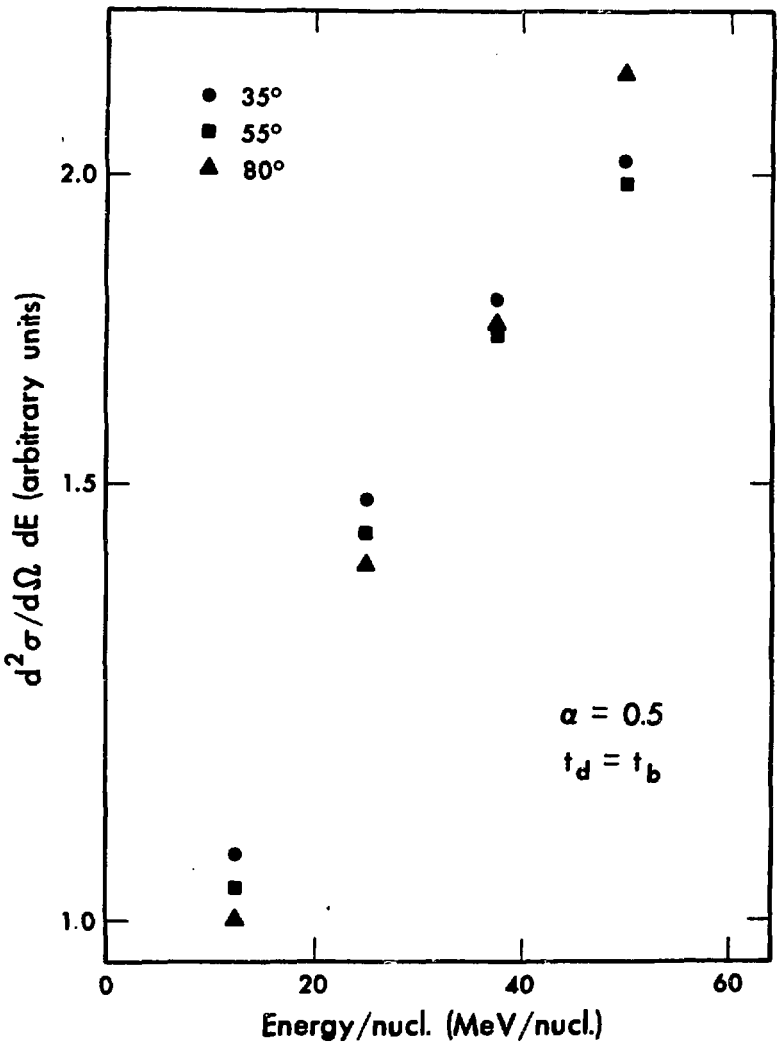
35°
55°
80°
2.0
1.5
1.0
$d^2\sigma/d\Omega\ dE$ (arbitrary units)
$\alpha = 0.5$
$t_d = t_b$
0
20
40
60
Energy/nucl. (MeV/nucl.)

Fig. 15

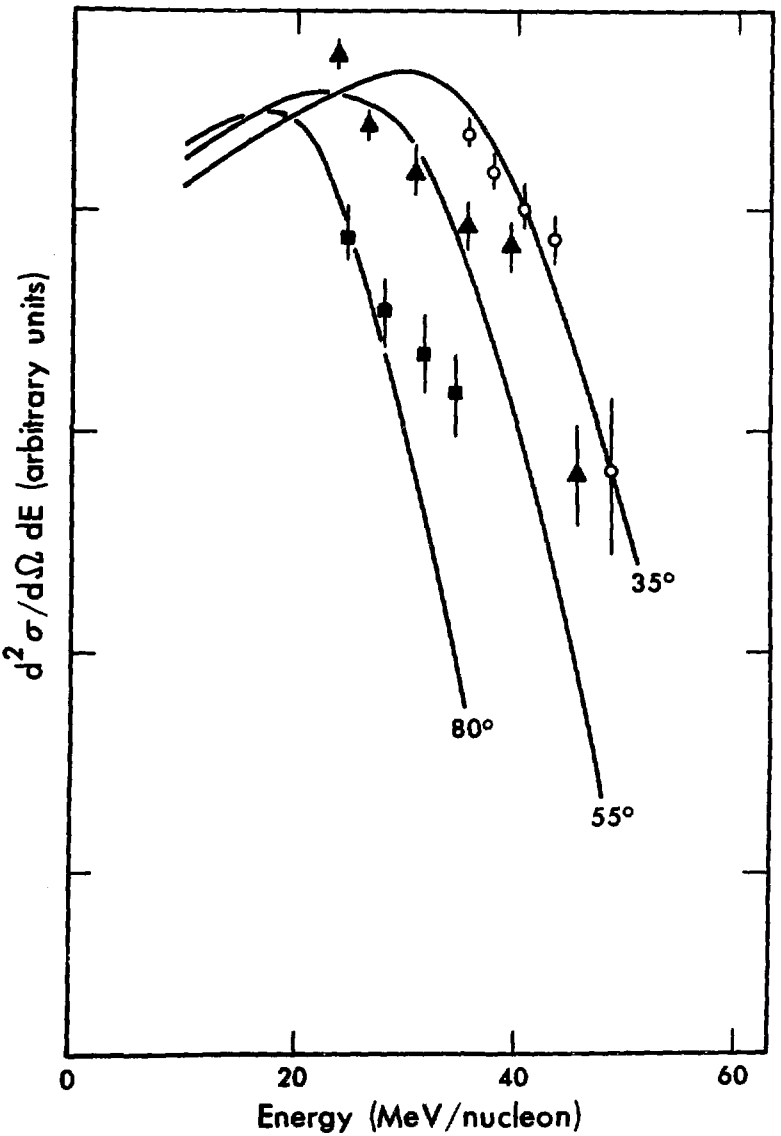
d²σ/dΩ dE (arbitrary units)
35°
80°
55°
0
20
40
60
Energy (MeV/nucleon)

Fig. 16

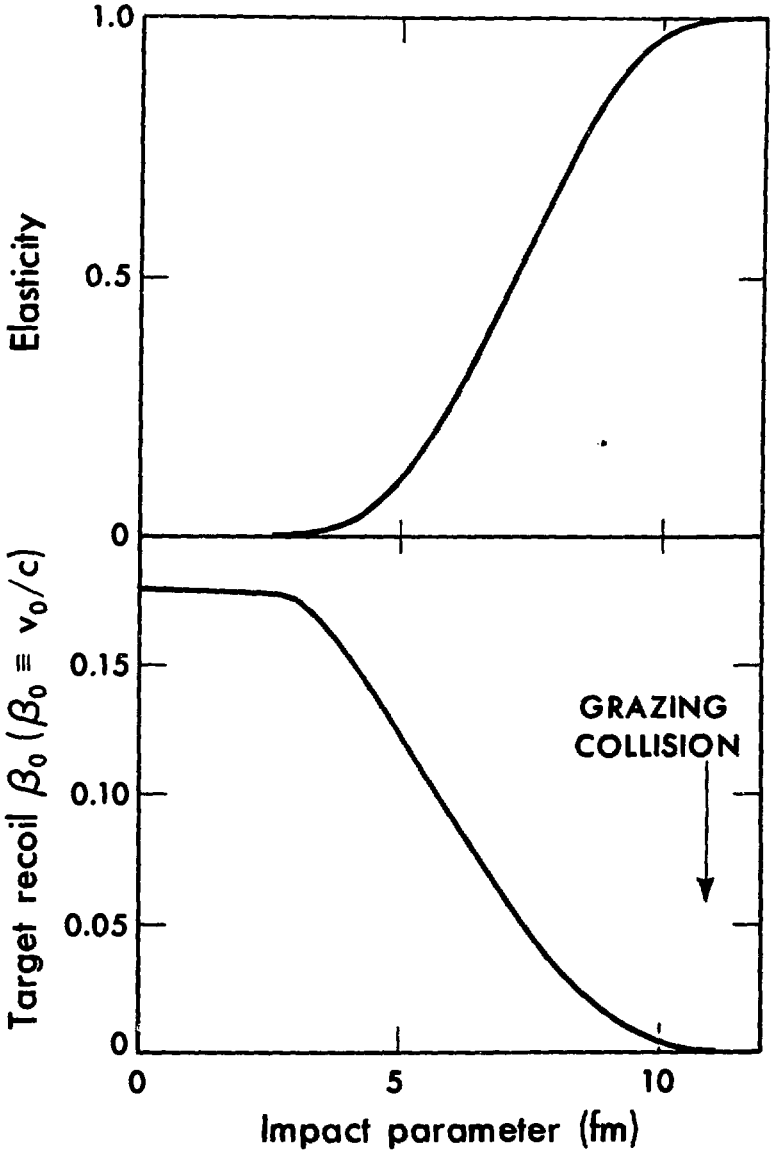
1.0
0.5
0
Elasticity
0.15
0.10
0.05
0
Target recoil β_0 ($\beta_0 \equiv v_0/c$)
GRAZING
COLLISION
0
5
10
Impact parameter (fm)

Fig. 17(a)

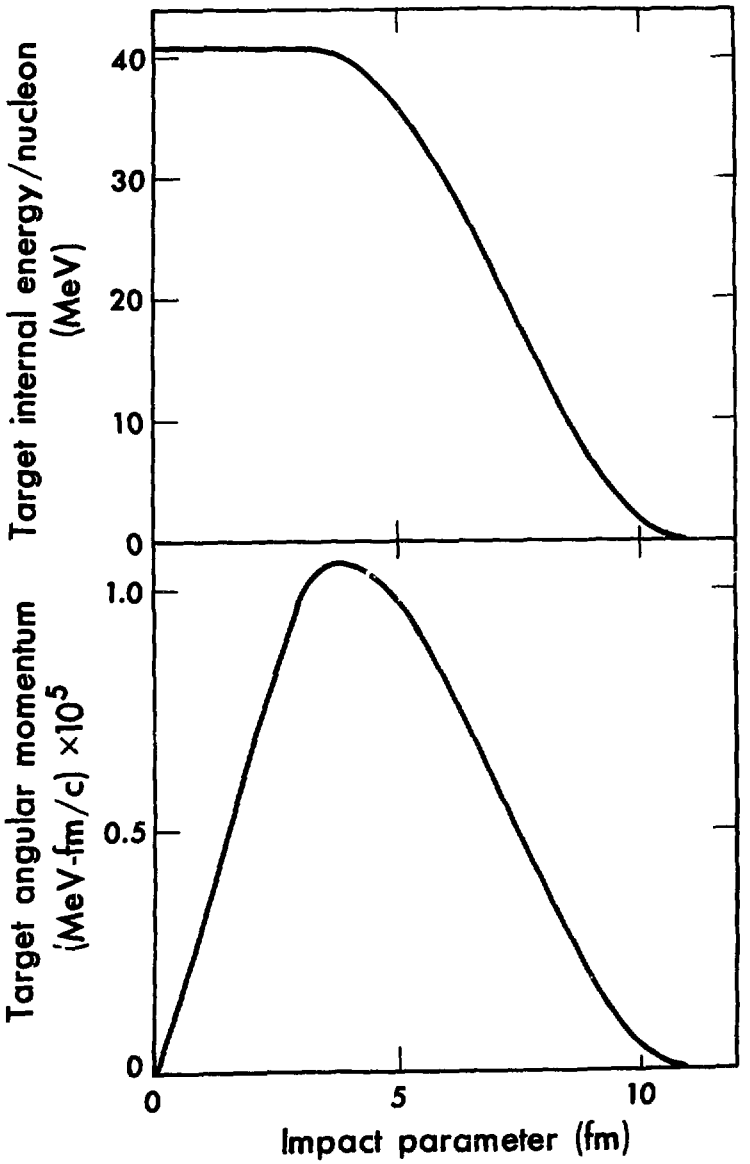
Target internal energy/nucleon (MeV)
40
30
20
10
0
Target angular momentum (MeV-fm/c) ×10^5
1.0
0.5
0
0
5
10
Impact parameter (fm)

Fig. 17(b)

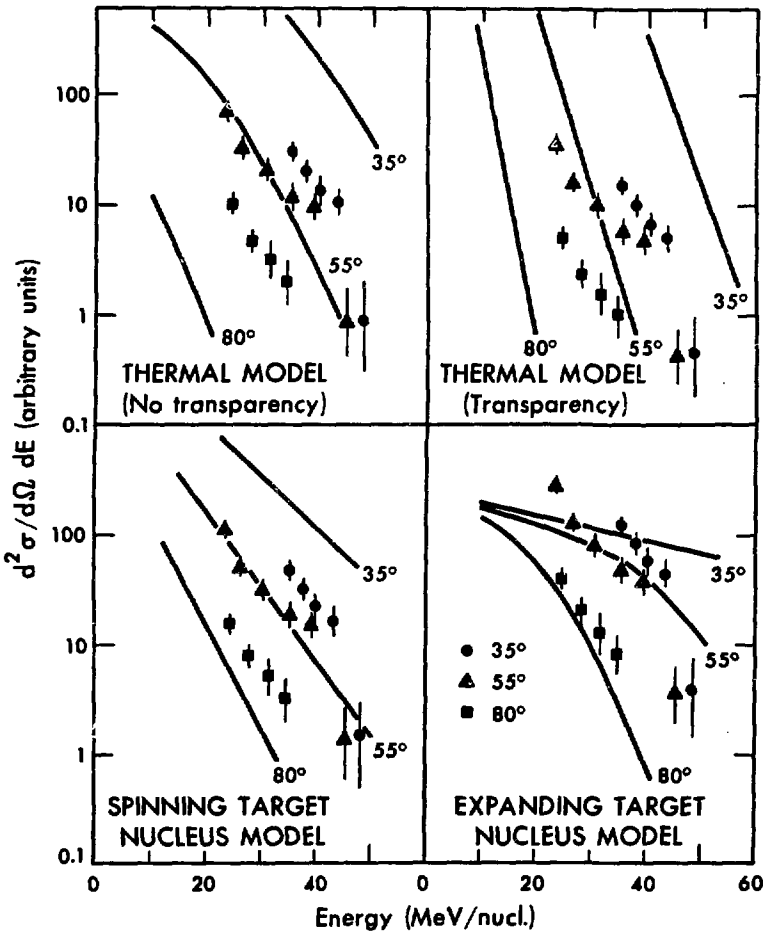
THERMAL MODEL
(No transparency)
THERMAL MODEL
(Transparency)
SPINNING TARGET
NUCLEUS MODEL
EXPANDING TARGET
NUCLEUS MODEL
35°
55°
80°
d²σ/dΩ dE (arbitrary units)
Energy (MeV/nucl.)

Fig. 18

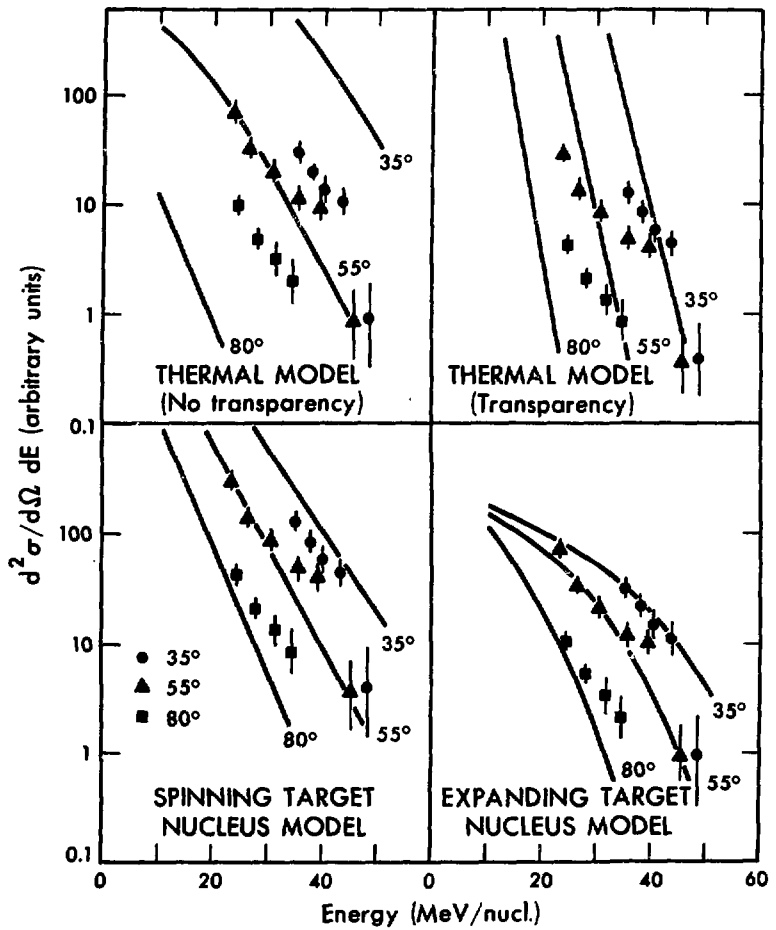
100
10
1
0.1
35°
55°
80°
THERMAL MODEL
(No transparency)
THERMAL MODEL
(Transparency)
35°
55°
80°
d²σ/dΩ dE (arbitrary units)
35°
55°
80°
SPINNING TARGET
NUCLEUS MODEL
EXPANDING TARGET
NUCLEUS MODEL
0
20
40
60
Energy (MeV/nucl.)

Fig. 19

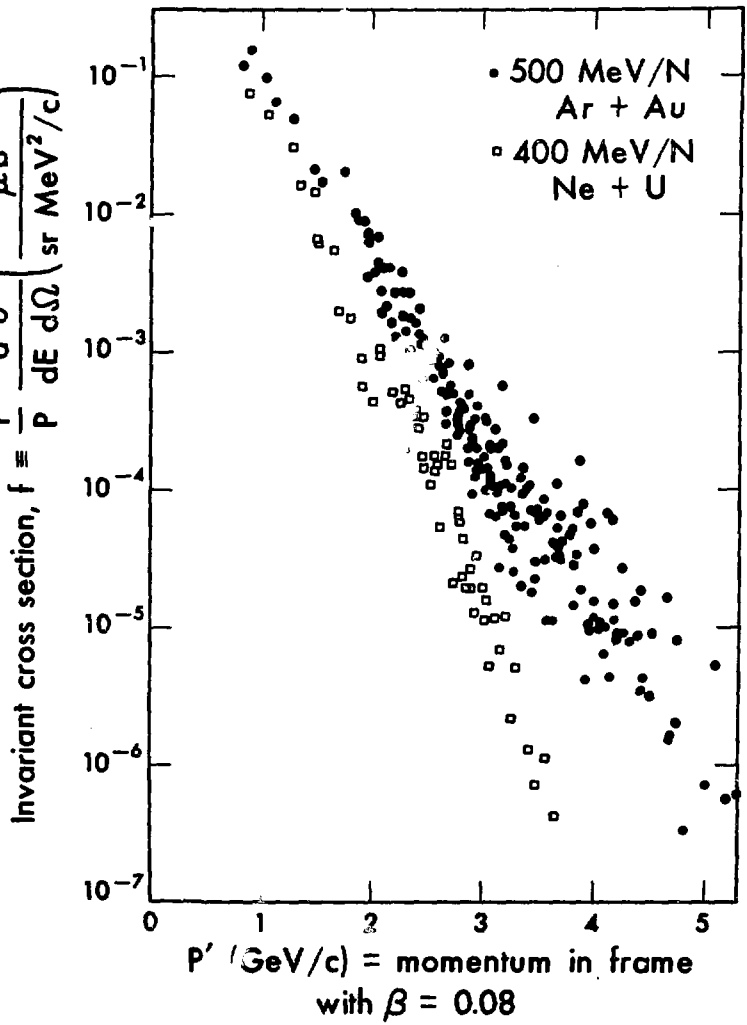
• 500 MeV/N
Ar + Au
▫ 400 MeV/N
Ne + U
Invariant cross section, $f \equiv \frac{1}{P}\frac{d^2\sigma}{dE\, d\Omega}\left(\frac{\mu b}{sr\ MeV^2/c}\right)$
10^{-1}
10^{-2}
10^{-3}
10^{-4}
10^{-5}
10^{-6}
10^{-7}
0
1
2
3
4
5
P' (GeV/c) = momentum in frame
with β = 0.08

Fig. 20

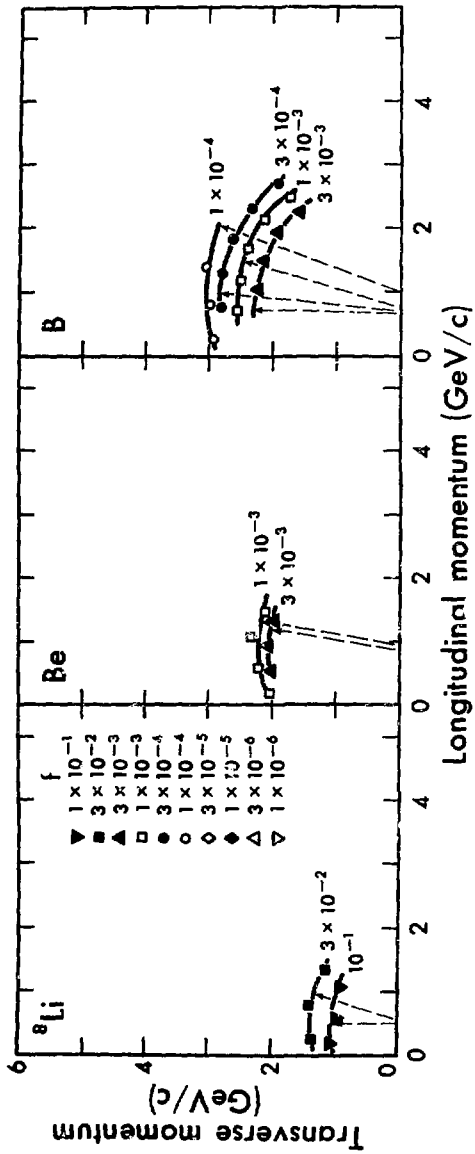
Transverse momentum (GeV/c)
Longitudinal momentum (GeV/c)
^{8}Li
Be
B
f
1 × 10^{-1}
3 × 10^{-2}
3 × 10^{-3}
1 × 10^{-3}
3 × 10^{-4}
1 × 10^{-4}
3 × 10^{-5}
1 × 10^{-5}
3 × 10^{-6}
1 × 10^{-6}
3 × 10^{-2}
10^{-1}
1 × 10^{-3}
3 × 10^{-3}
1 × 10^{-4}
3 × 10^{-4}
1 × 10^{-3}
3 × 10^{-3}

Fig. 21(a)

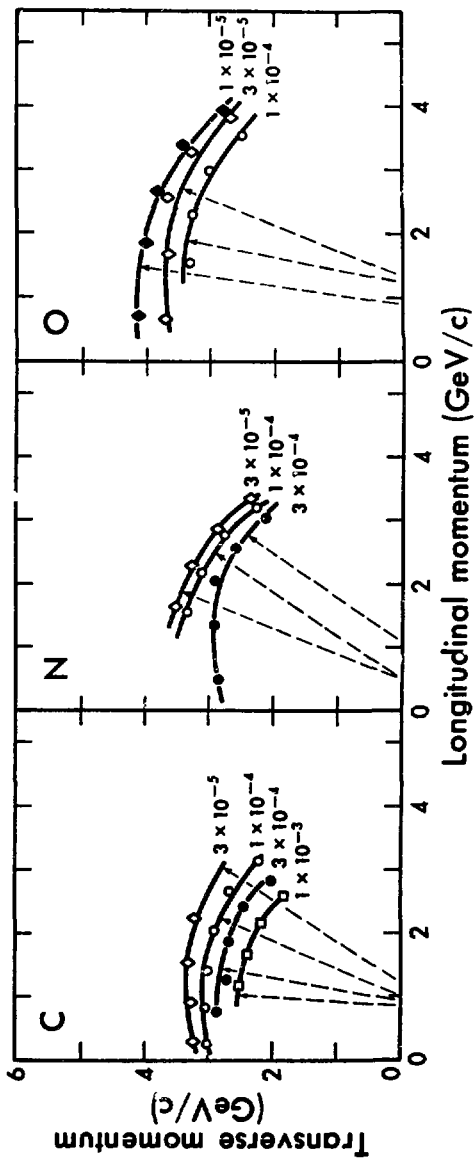
C
N
O
3×10^{-5}
1×10^{-4}
3×10^{-4}
1×10^{-3}
1×10^{-5}
3×10^{-5}
1×10^{-4}
Transverse momentum (GeV/c)
Longitudinal momentum (GeV/c)
0
2
4
6

Fig. 21(b)

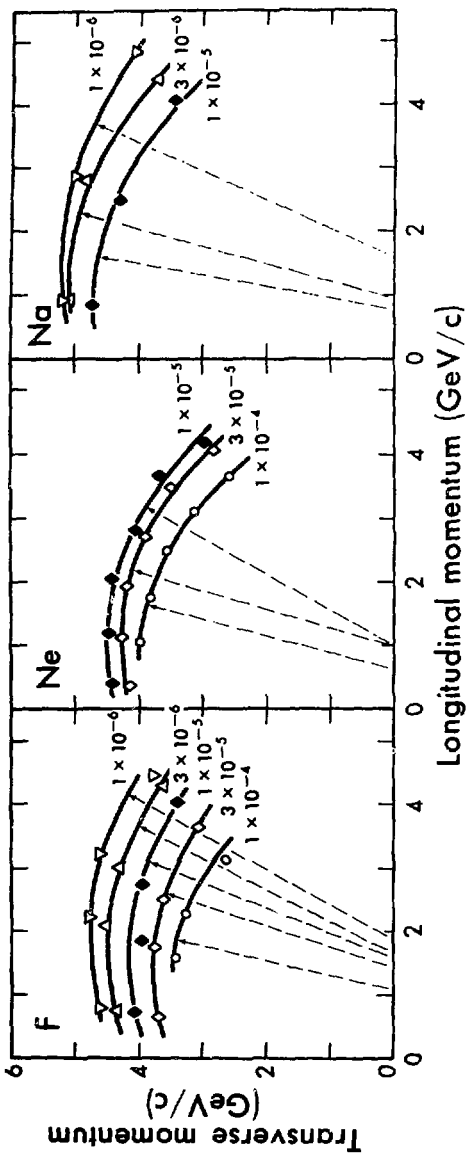
Transverse momentum (GeV/c)
Longitudinal momentum (GeV/c)
F
Ne
Na
1 × 10⁻⁶
3 × 10⁻⁶
1 × 10⁻⁵
3 × 10⁻⁵
1 × 10⁻⁴
0
2
4
6

Fig. 21(c)

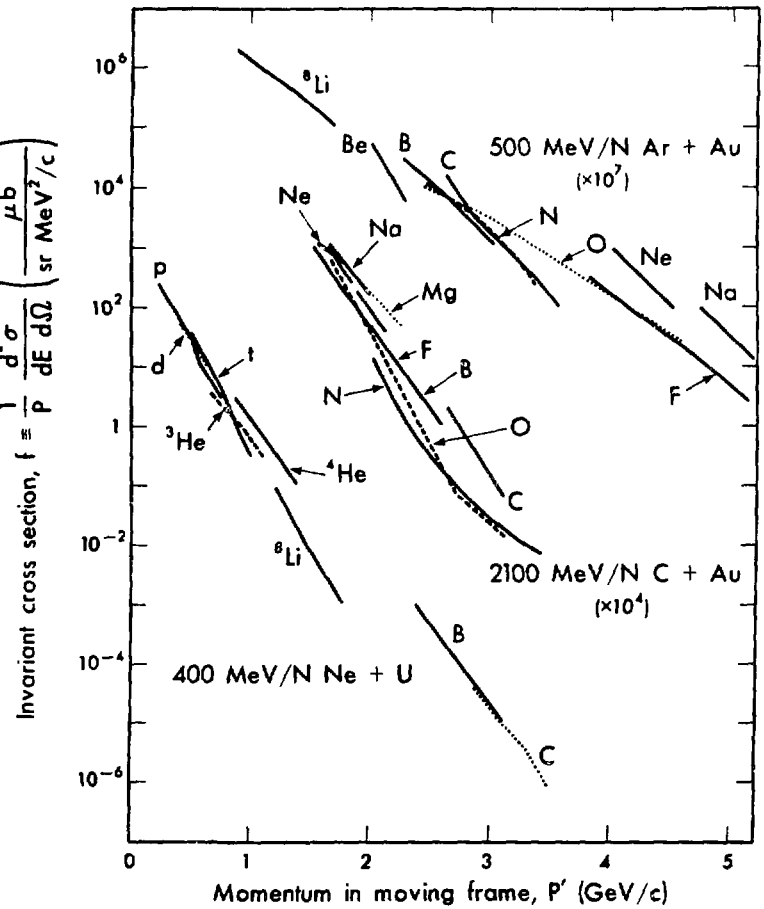
Invariant cross section, $f \equiv \frac{1}{P}\frac{d^2\sigma}{dE\,d\Omega}\left(\frac{\mu b}{sr\ MeV^2/c}\right)$
Momentum in moving frame, P' (GeV/c)
500 MeV/N Ar + Au
(×10⁷)
2100 MeV/N C + Au
(×10⁴)
400 MeV/N Ne + U
⁸Li
Be
B
C
N
O
Ne
Na
F
Mg
p
d
t
³He
⁴He

Fig. 22